OPTIMIZING GRAPHENE OXIDE REDUCTION VIA LASER IRRADIATION

By

Austin Patrick Osenga

December 2016

Thesis advisor: Dr. John M. Kenney

Major Department: Physics

Abstract

Graphene is a very promising material for electronics, that enables a large amount of new applications, but direct methods to engineer graphene-based electronics are very costly. This thesis discusses a single step method to reduce graphene oxide via laser irradiation, costing approximately five cents per component. This was accomplished using a computer numerically controlled laser engraver equipped with a 450nm laser diode. Reduced graphene oxide samples were prepared on a polycarbonate substrate at various laser powers, scan speeds, and total energy deposition, in an attempt to optimize this single step reduction. The quality of the finished product was determined by two probe multimeter resistance measurements, and carbon to oxygen ratios given by X-ray microanalysis. Optimal reduction was achieved at scan speeds greater than 8 mm/s and laser powers exceeding 200 mW.

OPTIMIZING GRAPHENE OXIDE REDUCTION VIA LASER IRRADIATION

A Thesis

Presented To The Faculty of the Department of Department of Physics

East Carolina University

In Partial Fulfillment of the Requirements for the Degree

Masters of Science in Physics

By

Austin Patrick Osenga

December 2016

OPTIMIZING GRAPHENE OXIDE REDUCTION VIA LASER IRRADIATION

By

Austin P. Osenga

APPROVED BY:

DIRECTOR OF THESIS: _____
John M Kenney, PhD

COMMITTEE MEMBER: _____
Regina DeWitt, PhD

COMMITTEE MEMBER: _____
Jefferson Shinpaugh, PhD

COMMITTEE MEMBER: _____
Anthony Kennedy, PhD

CHAIR OF THE DEPARTMENT
OF PHYSICS: _____
Jefferson Shinpaugh, PhD

DEAN OF THE
GRADUATE SCHOOL: _____
Paul Gemperline, PhD

ACKNOWLEDGEMENTS

I would like to thank my advisor Dr. John M. Kenney, for our weekly meetings pointing me in the right direction throughout this project. He encouraged me to adopt a skeptical scientific mind-set, and provided me with invaluable feedback and criticism on how I can improve many experimental methods. He also coached me in many ways on giving effective presentations to a scientific community. I also want to thank my committee members Dr. Anthony Kennedy, Dr. Regina DeWitt, and Dr. Jefferson Shinpaugh for their input on how my experimentation and research can provide a wholesome and complete story of this project.

I am grateful for Dr. Thomas Fink for teaching me the skills necessary to use the university Scanning Electron Microscope. This research would not have been possible without him. Dr. Orville Day recognized my passion for this field of research and helped me bring this project from my kitchen to an academic environment. My colleague Zachary Sherman-Burke helped me with many experiments and gave me several exciting ideas for furthering this research.

Finally, I wish to thank the physics support faculty Mr. William Holland, Mr. Gene Oakley, Mr. Mike Pawluch, and Dr. Kenneth Jacobs for helping me through the engineering learning curve in building a CNC, as I am forever indebted to them.

TABLE OF CONTENTS

LIST OF TABLES

LIST OF FIGURES

CHAPTER 1: INTRODUCTION

In 2004 the discovery of graphene by Novoselov marked what many would say to be a material science revolution (Geim & Novoselov, 2010). Graphene is a one atom thick honeycomb shaped monoatomic lattice made up of carbon atoms (Murray-Smith, 2013). It was discovered by adhering scotch tape to the surface of a chunk of graphite and peeling it off, leaving a thin piece of graphite stuck to the tape. Another piece of tape was used to peel off layers from the first piece of tape, yielding a thinner flake of graphite. Eventually after many iterations of this "scotch tape method" Andre Geim and Konstantin Novoselov finally obtained the first ever sample of single layer graphene. Six years later in 2010 Geim and Novoselov would be awarded a nobel prize for their ingeniously simple discovery (Geim & Novoselov, 2010). This made it possible for researchers to work with single atomic layers in laboratory environments (Murray-Smith, 2013).

Graphene has a myriad of wonderful properties that when exploited may change the developed world as we know it. This material has a tensile strength of 130 GPa (Lee, Wei, Kysar, & James, 2008), which is more than one hundred times stronger than steel, and yet, at 2.25 g/cm^3 (Liu, Xie, Zhang, Zheng, & Xu, 2012), it is five times less dense. For example, a one square meter hammock of graphene would be able to support the weight of a typical domestic cat while weighing less than one of its whiskers (Geim & Novoselov, 2010). Graphene's thermal conductivity is reported to be as high as 5300 W/m/K (Balandin, et al., 2008), which is ten times more efficient at transporting heat than any metal. With a conductivity of $1.1\times10^6/(\Omega\times m)$, it is at least twice as conductive as copper (Mendoza, 2012).

Some important applications of this wonder material include, but are not limited to advancing water purifiers, computers, building materials, sensors, protective coatings, super capacitors, and bionics (Murray-Smith, 2013). The main hurdle to overcome before we begin to see graphene on a day-to-day basis is commercialization. A cost effective method to manufacture pristine graphene on a large scale has yet to be discovered (Murray-Smith, 2013).

A promising starting material for a cost effective synthesis of graphene is called graphene oxide (GO). The earliest reports of GO can be traced back to the 1840's when German scientist Schafhaeutl reported the intercalation and exfoliation of graphite with sulfuric and nitric acids (Chua & Pumera, 2014). Graphene oxide is similar to graphene in that it is single layer. However, the hexagonal lattice is discontinuous in GO because oxygen-containing functional groups hog some of the carbons valence electrons preventing them from sp^2 hybridizing with neighboring carbon atoms. GO serves as a good candidate for a starting point in the synthesis of graphene because it is inexpensive to manufacture, and it is water-soluble.

Researchers have tried many methods of reducing graphene oxide to graphene. For formality purposes, the rest of this paper will refer to the reduced product of graphene oxide to "reduced graphene oxide (rGO)" and not graphene because that would imply the reduction was perfect, and this has not been achieved yet. GO has been reduced by means of chemical, optical, and thermal methods (Pei & Cheng, 2011). This thesis will discuss a technique for thermally reducing GO via laser irradiation. Laser reduction was chosen because experimental variables are easily manipulated to optimize this reduction process. Also laser scribing offers a high-resolution approach for patterning rGO, and an engraving

device can imprint a 2D electrical circuit on a wide variety of substrates. Optimizing this method of reduction can provide a route to highly customized flexible soft-circuits on materials that were long thought to have no business in electronics.

Imprinting 2D circuits via lasers began to make its emergence in the scientific community in 2012 (El-Kady, Strong, Dubin, & Kaner, 2012). Various factors in optimizing this reduction mechanism include incident energy, wavelength, and scan speed. The general approach for this experiment uses a laser mounted to a computer numerical controlled (CNC) machine to reduce a sample of GO. The graphene oxide is dissolved in deionized water and drop-casted on a substrate and allowed to dry 24 hours prior to laser treatment. The CNC can then engrave virtually any pattern that fits the user's needs, explaining the need for optimizing this mechanism.

The following chapters of the thesis will discuss theory, materials and methods, results, and conclusions. The second chapter on theory will describe how lasers work, and characteristics of GO and graphene. The following third chapter will describe the methods and materials used in this experiment, along with many experimental variables adjusted in an attempt to optimize the reduction process.

The end of the materials and methods chapter will discuss how the starting and finished product was characterized. This chapter will include insight on how the many factors in this research affect the carbon to oxygen ratio and conductivity of the rGO. The final chapter will conclude with a summary of this work and areas of future research where this work can be furthered.

CHAPTER 2: OVERVIEW OF GRAPHITIC MATERIALS

This chapter formally discusses the structure and properties of graphitic like materials, and how they have been studied over the past one and a half centuries. Graphite is made up of several layered graphene sheets held together by van der Waals forces. A chemical procedure known as Hummer's method attaches oxygen functional groups to the graphene layers, which expands the distance between them and allows for easier separation of individual sheets (Chua & Pumera, 2014). The oxygen containing graphene layers are known as graphene oxide (GO). Graphene oxide can then be reduced by a variety of ways to remove the oxygen moieties and achieve highly conductive graphene like materials.

2.1 - Graphene/Graphite Oxide properties

Graphene oxide is most commonly synthesized by a modified Hummer's method yielding graphite oxide, followed by sonication, which produces graphene oxide (Chua & Pumera, 2014). If graphene oxide is more than three layers it is referred to as graphite oxide (Pei & Cheng, 2011). Typically graphene oxide will have a carbon to oxygen ratio of approximately 1.5 to 2.5 (Chua & Pumera, 2014). Despite the synthesis of graphite oxide being known for nearly 150 years, the exact molecular structure remains unknown (Chua & Pumera, 2014). Several structures for graphite oxide have been proposed over the years. Seven accepted structures are shown in Figure 1 with Ajayan's model being one of the most widely accepted (Chua & Pumera, 2014).

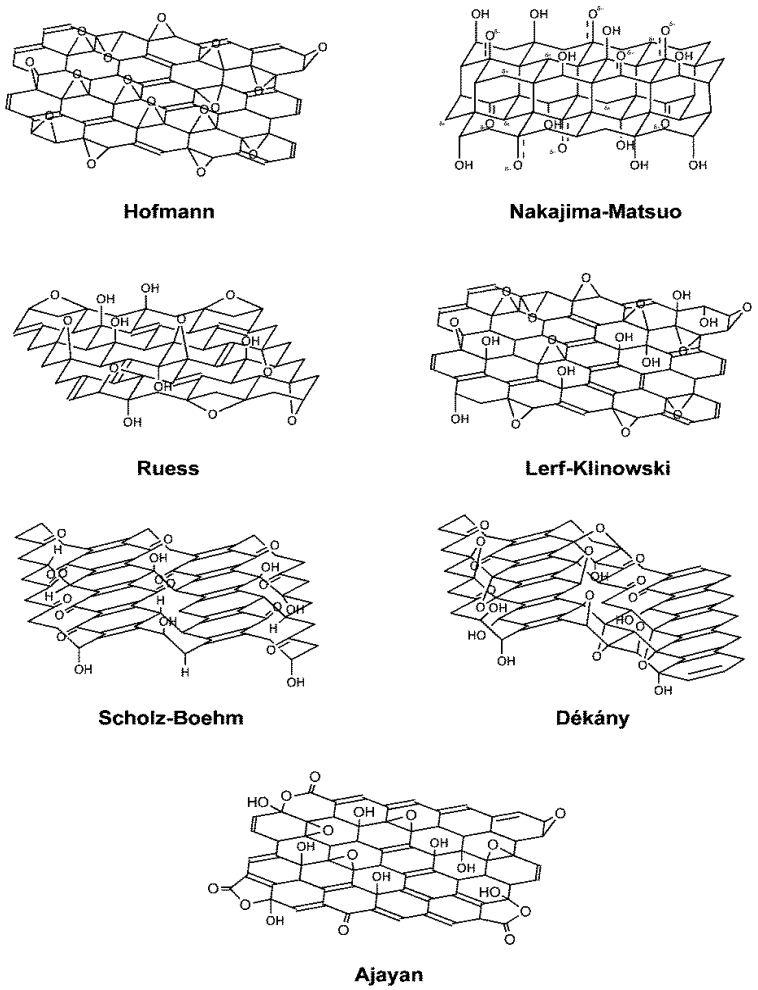

Figure 1 Seven proposed structures of graphene oxide (Chua & Pumera, 2014). The bottom structure is Ajayan's model of GO.

Ajayan and co-workers determined the relative ratios of the oxygen containing functional groups to be 115 (hydroxyl and epoxide): 3 (lactol O-C-O): 63(graphitic sp^2 carbon): 10 (lactol + ester + acid carbonyl): 9 (ketone carbonyl) (Chua & Pumera, 2014). When graphite is oxidized with oxygen containing functional groups, the interlayer spacing between graphene sheets is increased from ~0.3 nm to ~0.8 nm (Chua & Pumera, 2014), which promotes easy exfoliation (Murray-Smith, 2013). This occurs because the oxygen groups intercalate the graphite, weakening their strong van der Waals forces between

sheets. Note that graphene oxide and graphite oxide are nearly synonymous with one another because we are only considering ten layers or less. Their synthesis is chemically identical until the final step where sonication occurs breaking the graphite oxide into sheets of three layers or less. One should now realize that oxidizing graphitic compounds provides an easy method to work with nearly single atomic layers. What's left is to reduce it back to graphene. The term reduction is often defined as the gain of electrons or increase in oxidation number by inorganic chemists. This paper will follow the organic chemist's definition of reduction referring to the loss of oxygen or gain of hydrogen. It wasn't until 80 years after the first preparation of graphite oxide when scientists attempted to remove the oxygen functionalities from the surface of graphite oxide (Chua & Pumera, 2014).

2.2 - Graphene properties

As mentioned earlier graphene is a two-dimensional material made up of single layer carbon arranged in a honeycomb or chicken wire lattice as shown in **Figure 2**.

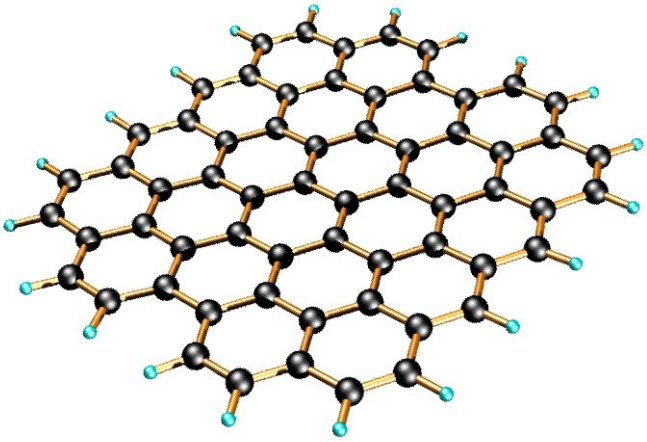

Figure 2 Hexagonal graphene lattice structure (Murray-Smith, 2013).

Along with being one of the strongest materials, this is also the thinnest material known to human kind. The term graphene comes from a combination of graphite and the suffix –ene by Hanns-Peter Boehm in 1962 due to the π-bonded nature provided by the $2p_z$ electrons (Murray-Smith, 2013). The bond length between neighboring carbon atoms is approximately 0.142 nanometers (Murray-Smith, 2013). When graphene sheets stack to form graphite, they are held together via strong van der Waals forces with an interplanar spacing of 0.335 nm (Murray-Smith, 2013). Graphene has conductivity of about 10^8 S/m where silver, copper, gold, and aluminum have lesser conductivities (Murray-Smith, 2013). Table 1 shows the conductivity of graphene compared to several other materials.

Table 1: Conductivity of several materials compared to graphene (Murray-Smith, 2013).

Material	**Electrical Conductivity ($S*m^{-1}$)**
Graphene	~10 to the power of 8
Silver	63.0×10^6
Copper	59.6×10^6
Annealed Copper	58.0×10^6
Gold	45.2×10^6
Aluminum	37.8×10^6
Sea water	4.8
Drinking water	0.0005 - 0.05
Deionized water	5.5×10^{-6}
Jet A – 1 Kerosene	50×10^{-12} - 450×10^{-12}
n-hexane	100×10^{-12}

Graphene's thermal conductivity has been measured at 4840-5300 W/(m×K), exceeding diamond's thermal conductivity of 900-2320 W/(m×K) (Balandin, et al., 2008). A comparison of graphene thermal conductivity with other materials is shown in Table 2.

Table 2: Thermal conductivity of graphene compared with other materials (Murray-Smith, 2013).

Material	**Thermal conductivity W/(m×K)**
Graphene	4840 – 5300
Diamond	900 – 2320
Silver	429
Copper	401
Gold	318
Aluminum (pure)	237

Graphene also has a breaking strength over 100 times greater than steel film of the same thickness (Lee, Wei, Kysar, & James, 2008). Put in perspective, a one square meter sheet of graphene would be able to support 4 kg while weighing only 0.77 mg (Geim & Novoselov, 2010).

Many of the wonderful properties of graphene are a result of its electronic structure. All of the carbon atoms in graphene are sp^2 hybridized. One 2s orbital hybridizes with the $2p_x$ and $2p_y$ orbitals to generate three σ-bonds to neighboring atoms making up the 2D hexagonal lattice in the x-y plane. There is one remaining unhybridized $2p_z$ orbital per carbon atom that is perpendicular to the x-y plane and form π-bonds with neighboring $2p_z$ orbitals. The π-bonds then hybridize together to form the π-band and π^*-bands. The $2p_z$

electronic states are delocalized providing graphene with its remarkable electron mobility of 15,000 $cm^2 \bullet V^{-1} \bullet s^{-1}$ at room temperature (Murray-Smith, 2013; Chun Kiang Chua, 2014; Songfeng Pei, 2011). Graphene is a zero band-gap semiconductor because its conduction and valence bands meet at the Dirac points (Geim & Novoselov, 2010).

In 1947 P. R. Wallace discovered an interesting phenomenon. The E-k relation is linear for low energies near the six corners of the 2D hexagonal Brillouin zone. This discovery leads to a zero effective mass for electrons and holes (Murray-Smith, 2013). A diagram showing this relation is displayed in Figure 3.

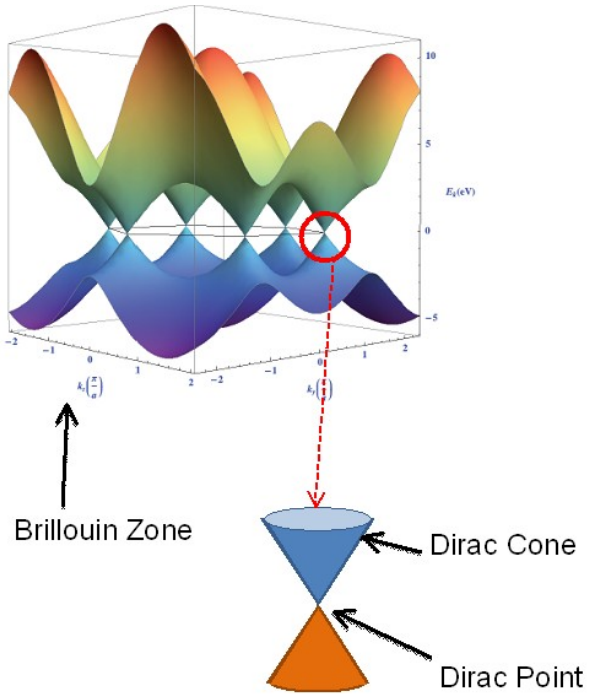

Figure 3 Linear E-k relation for low energies near the six corners of the Brillouin zone (Geim & Novoselov, 2010)

CHAPTER 3: LASER ENGRAVER BUILD

The goal was to develop a method for GO reduction with laser irradiation. The starting point of this experiment required the building of a computer numerically controlled machine (CNC) to which the laser was mounted. The result is shown in Figure 4.

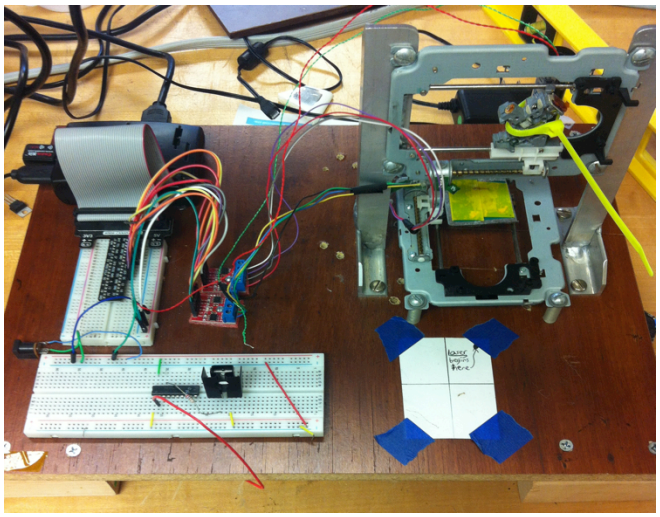

Figure 4 Computer Numerically Controlled machine (CNC) laser engraver.

The two-axis laser engraver build used a Raspberry pi B+, two L9110 dual H bridges, and two 4-wire 2-phase bipolar stepper motors. Two CD drives were salvaged from a desktop computer that contained the stepper motors. One CD drive was mounted horizontally on a level surface making up the X-axis. The Y-axis CD drive was mounted vertically above the X-axis, oriented perpendicular to the X-axis as shown in Figure 5.

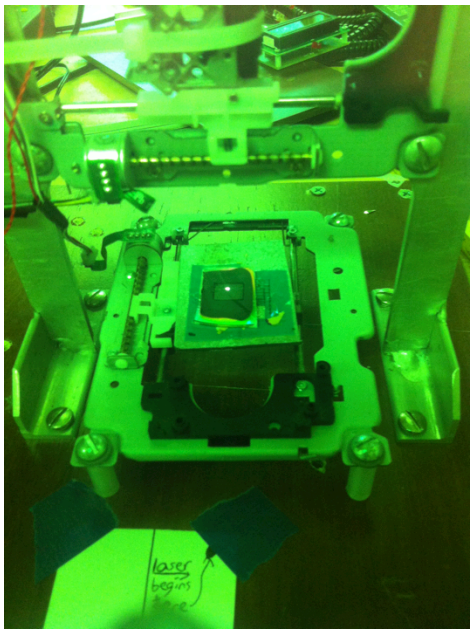

Figure 5 X (top) and Y (bottom) stepper motors mounted to CD drives oriented perpendicular to one another. A laser filter is responsible for the green tint in this image as to not over saturate the camera with too much light

That way one motor operates in the forward and backwards direction while the other operates in the left to right direction, giving the CNC two degrees of freedom. The motors were then soldered to two dual channel H-bridges shown in Figure 6.

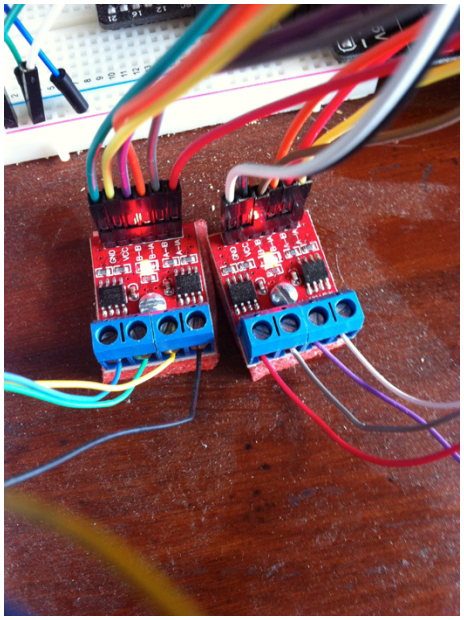

Figure 6 Two L9110 dual channel H-bridges connected to X and Y stepper motors.

An H-bridge is a circuit that contains four switches that can apply a voltage in both directions. One L9110 H-bridge contains two channels, which allow the stepper motor to operate in both directions via truly reversible voltage. A simple schematic of an H-bridge is shown in Figure 7.

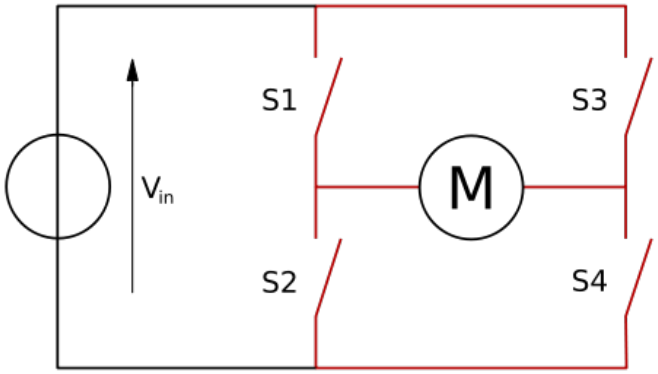

Figure 7 Circuit diagram of an H-bridge. When S1 and S4 are closed, voltage across M is towards the right. When S3 and S2 are closed, voltage across M is towards the left.

A total of four channels give the two degrees of freedom required for a two-axis CNC. The H-bridges were then connected to the raspberry pi's general-purpose input output (GPIO) pins where they could be interpreted by a python script (Douglas, 2014). The GPIO pins are connected via ribbon cable to a breadboard where jumper wires could then attach them to the H-bridges as displayed in Figure 8.

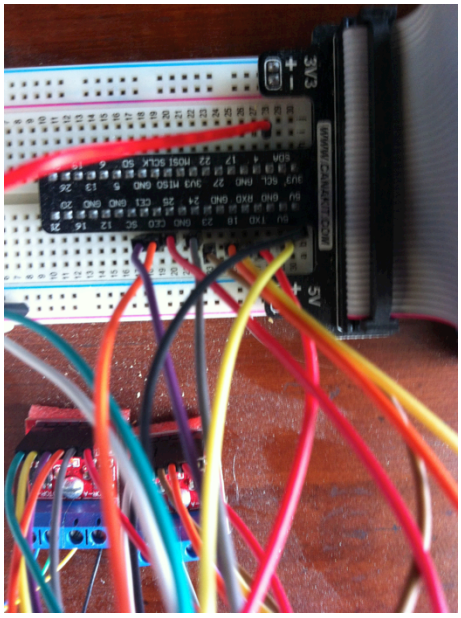

Figure 8 GPIO pins leading into the two dual channel H-bridges.

The python code contained information about the phase of the stepper motor and the position. Using only this script allows the user to manually control the motors by inputting the number of steps for each axis. An additional python script was compiled to interpret G-code. G-code is a programming language that is commonly used among 3D printers and tells the machine where to move, how fast to move, and what path to travel. G-code interpretation is important because it permits the use of vector editing software where the user can design virtually any pattern to be engraved on a 35 by 35 mm square. A single step from the motor moves the stage by a tenth of a millimeter. The vector editing software used in this experiment was Inkscape (Douglas, 2014). A screen shot of the Inkscape software is shown in Figure 9.

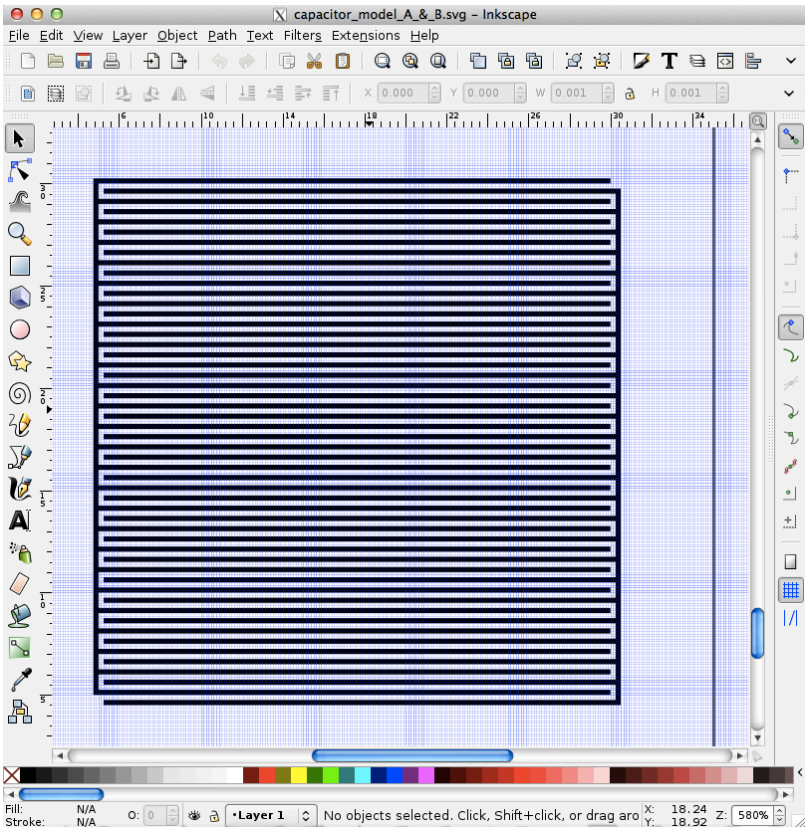

Figure 9 Inkscape vector editing software used for designing engravings.

A laser was then attached to the vertical Y-axis stage. The laser that was predominately used in this research was a PL TB450 solid-state laser diode. The 5.6mm laser diode has a max optical output of 1.4 W with a spectral width (FWHM) of 4 nm centered around 450 nm. The diode was then mounted in a 16x55mm focusable housing with glass lens. The beam was focused at 70 mm from the lens and profiled.

3.1 - Solid State Laser Profile:

As mentioned above, the laser used in this experiment was a PLTB450 solid-state laser diode. The band gap of this laser was calculated to be 2.76eV, which corresponds to an InGaN semiconducting material. The central wavelength of the PLTB450 laser diode is

450nm with a spectral width (FWHM) of 4nm. A graph relating laser power output to the amount of current supplied to the laser is given in Figure 10 using an Osram power meter.

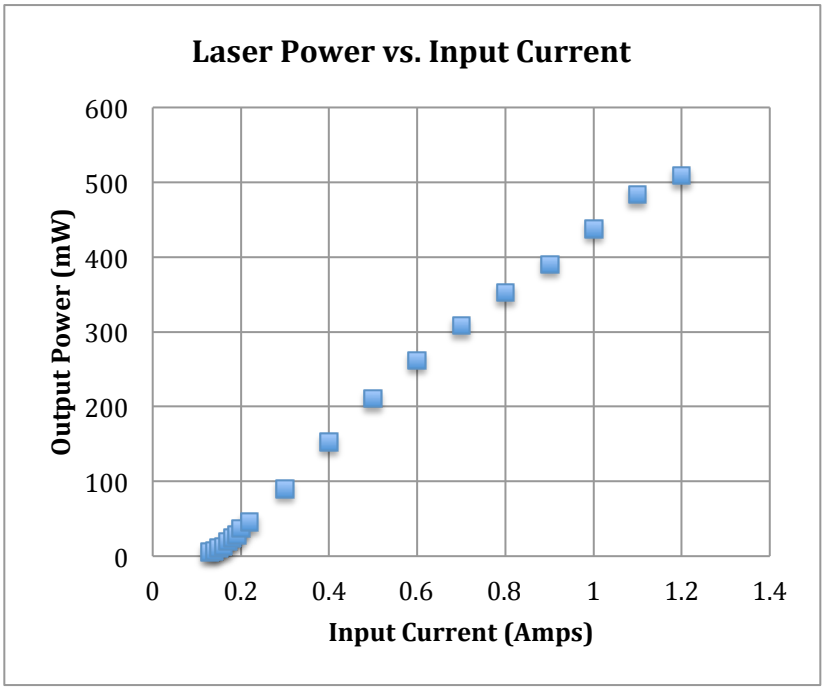

Figure 10 Laser power vs. input current measured by Osram power meter.

The laser was characterized using a BC106-vis camera with beam analyzing software from Thor Labs. The BC106-vis camera was placed at the laser focal length, 70mm from the laser lens. **Figure 11** shows a three-dimensional plot of intensity.

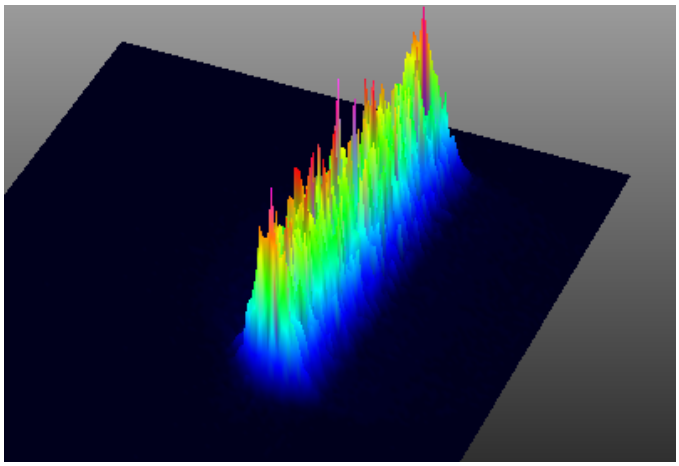

Figure 11 3D plot of intensity of PBL450 laser diode at twice the focal length.

The shape of the beam was highly elliptical with a 97.49% recorded eccentricity. The diameter of the major axis was measured at 686.15 micrometers where the minor axis was 152.84 micrometers. This corresponds to a beam cross-sectional area of 3.3×10^6 μm^2. Figure 12a and 12b shows a two-dimensional intensity plot of the minor and major axis of the beam cross-section.

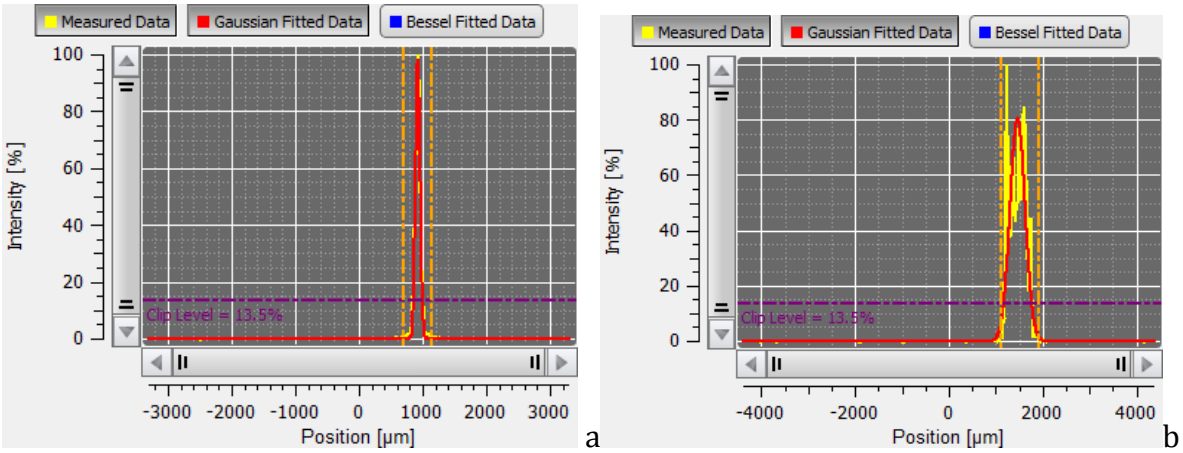

Figure 12 PBL450 450nm laser diode profile. Intensity[%] vs. Position[µm]. (a) Y- profile. (b) X-profile.

CHAPTER 4: MATERIALS AND METHODS

After determining the resolution of the CNC and profiling the laser, graphene oxide reduction could begin. The following method of reduction varies experimental parameters in an attempt to optimize conductivity and purity of the rGO product.

150 ml of Graphene oxide in an aqueous dispersion of deionized water concentrated at 5 mg/ml was purchased from Goographene. The approximate flake size of GO was about 1μm across with an average of three layers per flake provided by Goographene. The carbon to oxygen ratio of this GO was measured using the Quanta 200 X-ray microanalysis to be 2:1. The GO was deposited on a polycarbonate substrate via drop casting and allowed to dry under a fume hood for 24 hours.

The sample was then placed on the X-axis stage of the CNC and irradiated by a continuous wave 450-nm laser. Several 8.2mm by 10mm sheets were engraved. The first nine 8mm by 10mm sheets were engraved with a constant scan speed of 8 mm/second at different laser wattages. Samples 1-9 were exposed to 35mW, 90mW, 152mW, 211mW, 262mW, 308mW, 353mW, 390mW, and 437mW radiation respectively and shown in Table 3.

Table 3: Samples 1-9 with varying laser power at a constant scan speed.

Sample number	Laser Power (mW)	Scan speed (mm/s)	Total energy deposited (Joules)	Energy density (W/cm^2)
1	35	8	4	33.3
2	90	8	10.4	85.8
3	152	8	17.5	144.8
4	211	8	24.3	201.3
5	262	8	30.1	249.6
6	308	8	35.4	293.6
7	353	8	40.6	336.3
8	390	8	44.9	371.6
9	437	8	50.2	416.4

Nine additional 8.2mm by 10mm rGO sheet samples (10-18) were prepared using a constant laser wattage of 211mW with varying scan speeds. Sheets 10-18 were scanned at 2, 4, 6, 8, 10, 12, 16, 20, and 24 millimeters per second respectively and shown in Table 4.

Table 4: Samples 10-18 with varying scan speed with constant power.

Sample number	Laser Power (mW)	Scan speed (mm/s)	Total energy deposited (Joules)	Energy density (W/cm^2)
10	211	2	90.7	201.3
11	211	4	46.4	201.3
12	211	6	31.7	201.3
13	211	8	24.3	201.3
14	211	10	19.6	201.3
15	211	12	16.7	201.3
16	211	16	12.9	201.3
17	211	20	10.6	201.3
18	211	24	9.3	201.3

The intention of the first 18 samples was to determine if scan speed and/or power could be optimized for reduction. Six more sheets (19-24) were made all with the same total energy of 98 joules deposited. The first sample was scanned at 2 mm/second. The second was scanned twice at 4 mm/second. The third scanned three times at 6 mm/second. The speed was increased by 2 mm/second increments up to a final 12 mm/second sample scanned six times. Samples 19-24 are tabulated below in Table 5.

Table 5: Samples 19-14 have constant power and total energy with varied scan speed and number of scans.

Sample number	Laser Power (mW)	Scan speed (mm/s)	Number of scans	Total energy (Joules)	Energy density (W/cm^2)
19	211	2	1	98	201.3
20	211	4	2	98	201.3
21	211	6	3	98	201.3
22	211	8	4	98	201.3
23	211	10	5	98	201.3
24	211	12	6	98	201.3

The purpose of these samples is to determine if scan speed alone affected the quality of reduction considering that the total energy deposited remained the same, as the material has more time to cool down between several quick scans than one long scan.

4.1 - Characterization:

The reduction quality of these samples was determined by resistance measurements and carbon to oxygen ratios of the final material. Resistance measurements were taken with a two-probe multimeter. The resistance was measured with 1 cm spacing between probes across the 1 cm by 0.82 cm engraving 8 times and then averaged for each sample. Carbon to oxygen ratios were determined by an INCA X-ray microanalysis attachment to a Quanta 200 SEM. The atomic ratios of each sample was measured nine times at various scan sites and averaged. The standard error of these measurements ranged from 1.4 to 0.4. The

structure of the GO and rGO was imaged with the Quanta 200 SEM. A typical X-ray microanalysis spectrum of rGO is shown below in Figure 13.

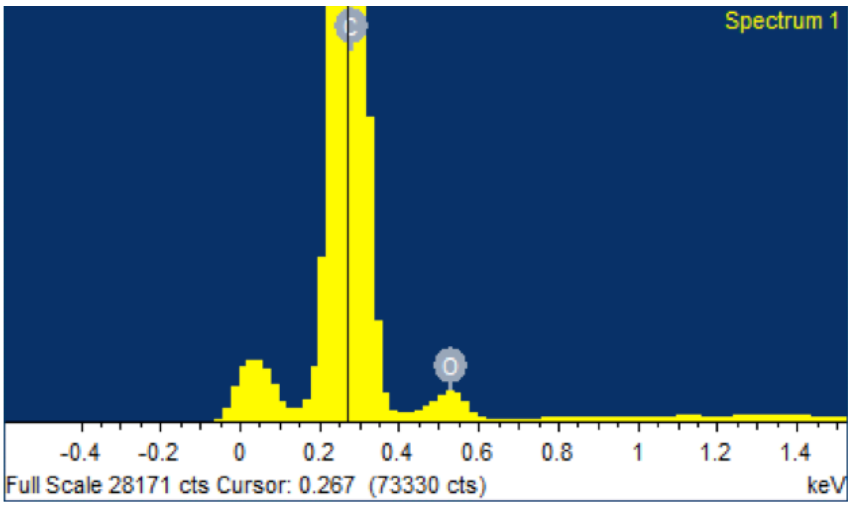

Figure 13 X-ray elemental analysis spectrum of rGO taken with INCA Silicon Drift Detector. Carbon peak is located at ~275 eV and oxygen peak is at ~550 eV.

Elemental analysis spectra are obtained when an incident electron beam ejects a K-shell electron from an atom where the vacancy is filled by an L-shell electron that emits a characteristic x-ray. The far left peak in the above spectrum is background noise, and is a result of bremsstrahlung occurring in the electron beam.

CHAPTER 5: RESULTS AND DISCUSSION

This chapter will address the quality of reduction taking place after laser treatment. Scan speed, laser power, and total energy deposition were adjusted and analyzed. A key observation influenced the polycarbonate substrate chosen for this research. GO was drop casted onto an aluminum oxide substrate and allowed to dry under a fume hood for 24 hours. After laser irradiation, the GO remained as an insulator and no visible changes were observed. Aluminum oxide having a high thermal conductivity of 35 W/(m×K) (City Plastics) likely behaves as a heat sink, not allowing the GO to reach temperatures high enough for reduction. Therefore, polycarbonate was chosen as a substrate because it has a low thermal conductivity of 0.19 W/(m×K), and can hold up longer in extreme temperatures (City Plastics). Since the laser used for reduction was not tuned to the bond energies of any oxygen containing functional groups, optical reduction can be ruled out. Thus, thermal reduction must be taking place.

5.1 - Varying Laser Power:

As mentioned above, rGO samples one through nine were produced by varying laser power at a constant scan speed of 8mm/second. A two-probe multimeter resistance measurement for each sample was taken 8 times, averaged, and plotted versus laser power as shown in Figure 10.

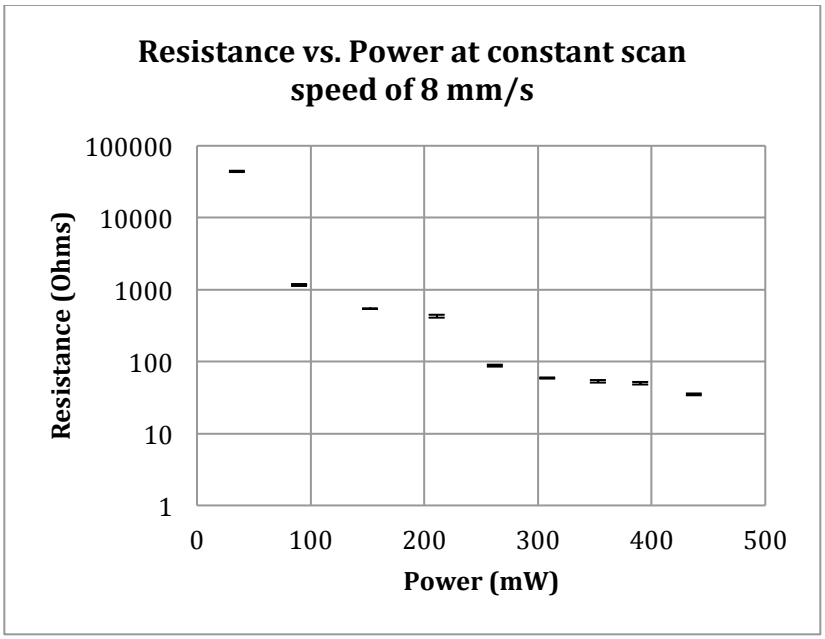

Figure 14 Resistance vs. Laser power at constant scan speed of 8 mm/s (samples 1-9). Note the logarithmic Y-axis. The points shown are actually error bars representing the standard error of the mean.

Firstly, note the logarithmic Y-axis on Figure 14, which allows for easier interpretation of the data. The plotted points are actually error bars given by the standard error of the mean of the measurements. **Figure 15** is the same data plotted without a logarithmic y-axis.

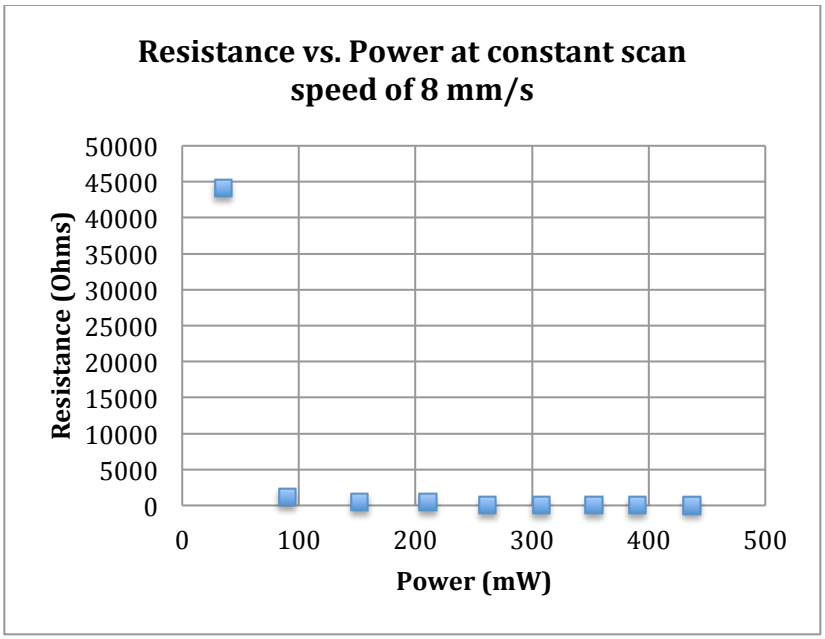

Figure 15 resistances vs. Laser powers at a constant scan speed of 8mm/s (samples 1-9), plotted with linear axis. Error bars representing the standard error of mean aren't visible as they are smaller than the displayed data points.

It can be seen from the figure above why this data is more easily interpretable when plotted with a logarithmic Y-axis. **Figure 15** at glance shows that the resistance begins to plateau after the first data point. However, Figure 14 shows a more truthful plot as we can see that resistance values begin to plateau at sub 100 Ω when the laser power exceeds 262 mW (5th data point). Even though the resistance values appear to flatten out after 262 mW, it should be noted that there is still slight decreasing resistance with increasing laser power. Additional data points at higher powers could not be obtained as the PLTB450 laser diode overheated and burned out at input currents greater than 1.2 Amps (see Figure 10). The PLTB450 laser diode was chosen for this experiment because it was the highest power laser compact enough to be mounted to the CNC. Following the trend in Figure 14,

one could hypothesize that data points at higher powers would lead to a continued decrease in resistance albeit slightly. If these additional data points would follow the same trend as shown in Figure 14 then one could argue that powers exceeding 300 mW would be inefficient in that the use of significant power would yield only a small decrease in resistance. On the contrary, experimental evidence is necessary to determine if the trend in Figure 14 would indeed continue to flatten out or if another critical point could be found at powers greater than 500 mW.

Figure 16 shows SEM images taken of rGO samples one through nine at 100x magnification.

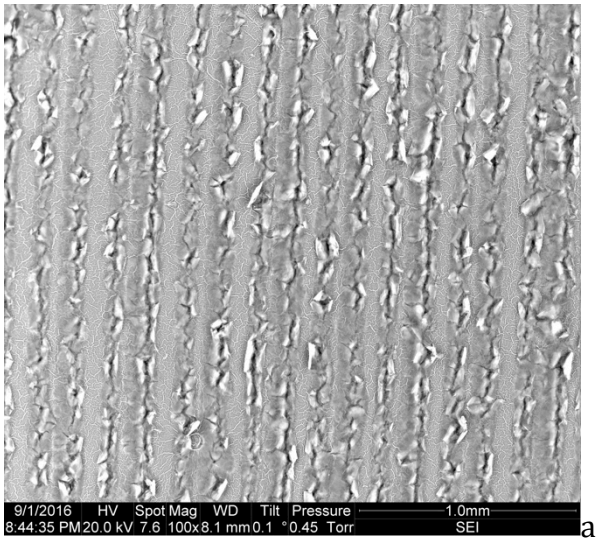

a

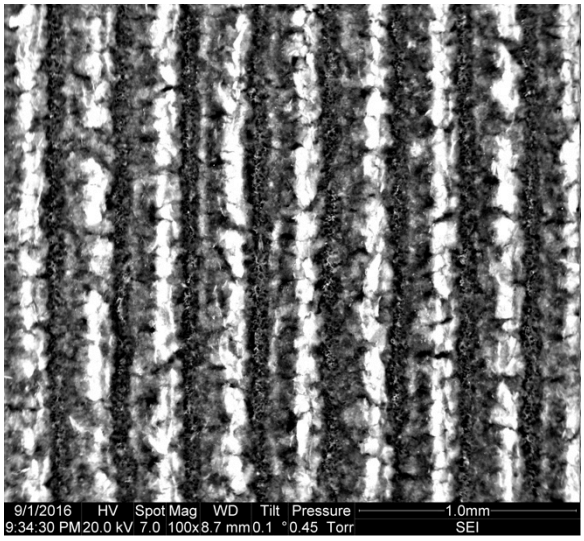

b

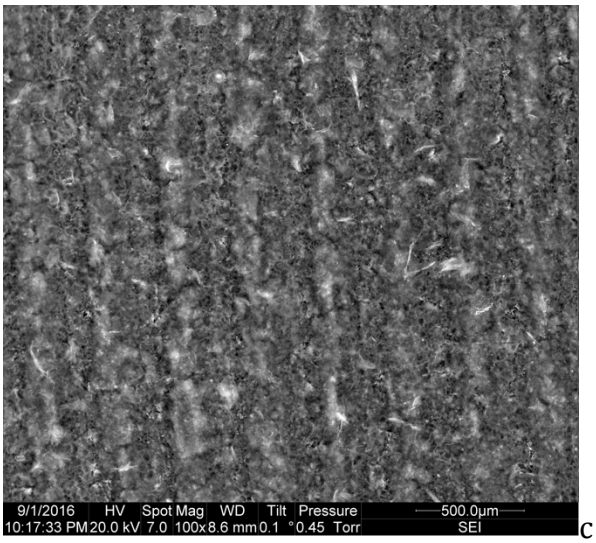
9/1/2016 HV Spot Mag WD Tilt Pressure 500.0µm
10:17:33 PM 20.0 kV 7.0 100x 8.6 mm 0.1 °0.45 Torr SEI
c

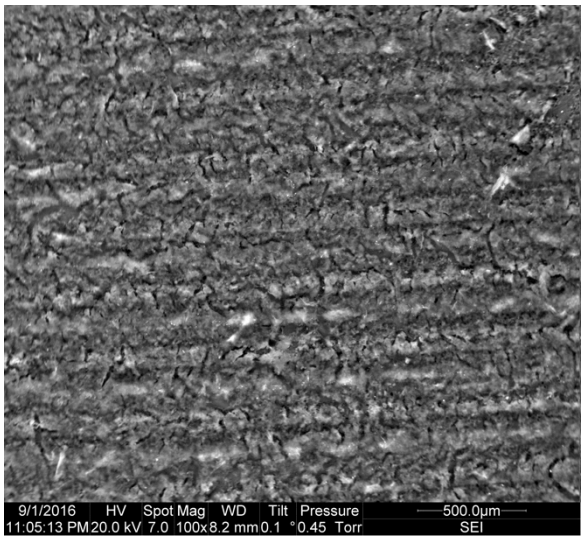
9/1/2016 HV Spot Mag WD Tilt Pressure 500.0µm
11:05:13 PM 20.0 kV 7.0 100x 8.2 mm 0.1 °0.45 Torr SEI
d

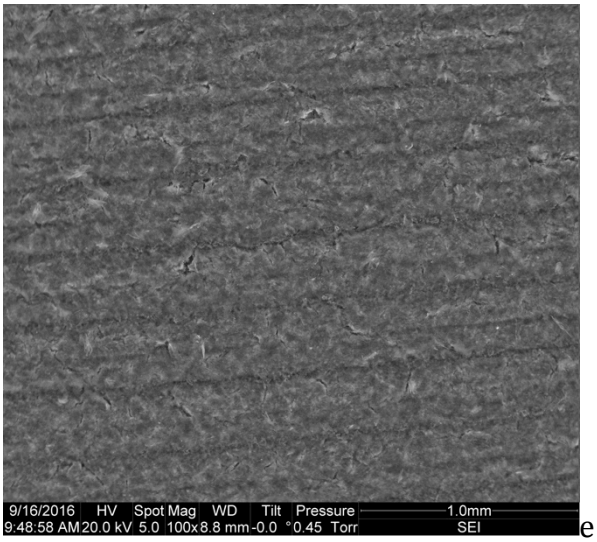
9/16/2016 HV Spot Mag WD Tilt Pressure 1.0mm
9:48:58 AM 20.0 kV 5.0 100x 8.8 mm -0.0 °0.45 Torr SEI
e

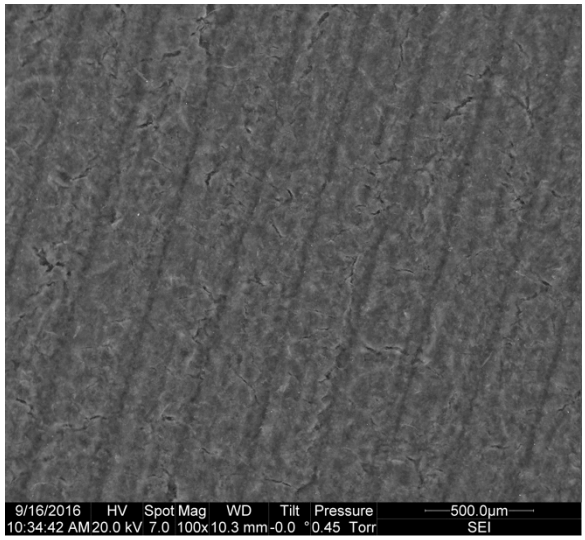
9/16/2016 HV Spot Mag WD Tilt Pressure 500.0µm
10:34:42 AM 20.0 kV 7.0 100x 10.3 mm -0.0 °0.45 Torr SEI
f

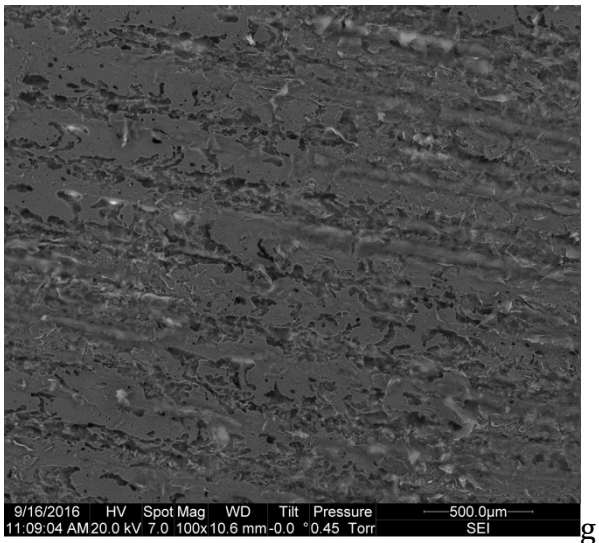
9/16/2016 HV Spot Mag WD Tilt Pressure 500.0µm
11:09:04 AM 20.0 kV 7.0 100x 10.6 mm -0.0 °0.45 Torr SEI
g

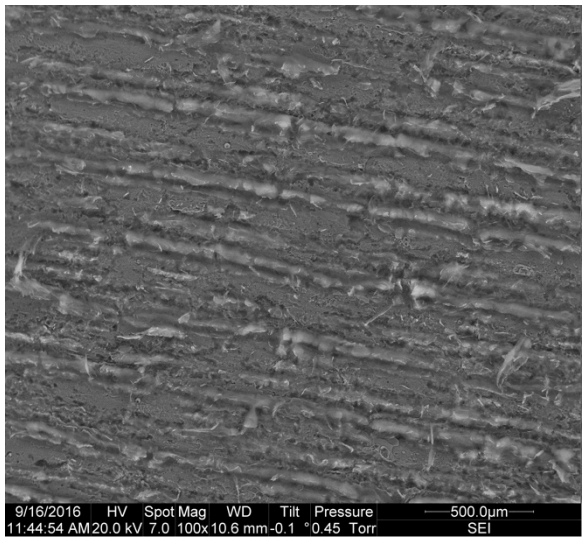
9/16/2016 HV Spot Mag WD Tilt Pressure 500.0µm
11:44:54 AM 20.0 kV 7.0 100x 10.6 mm -0.1 °0.45 Torr SEI
h

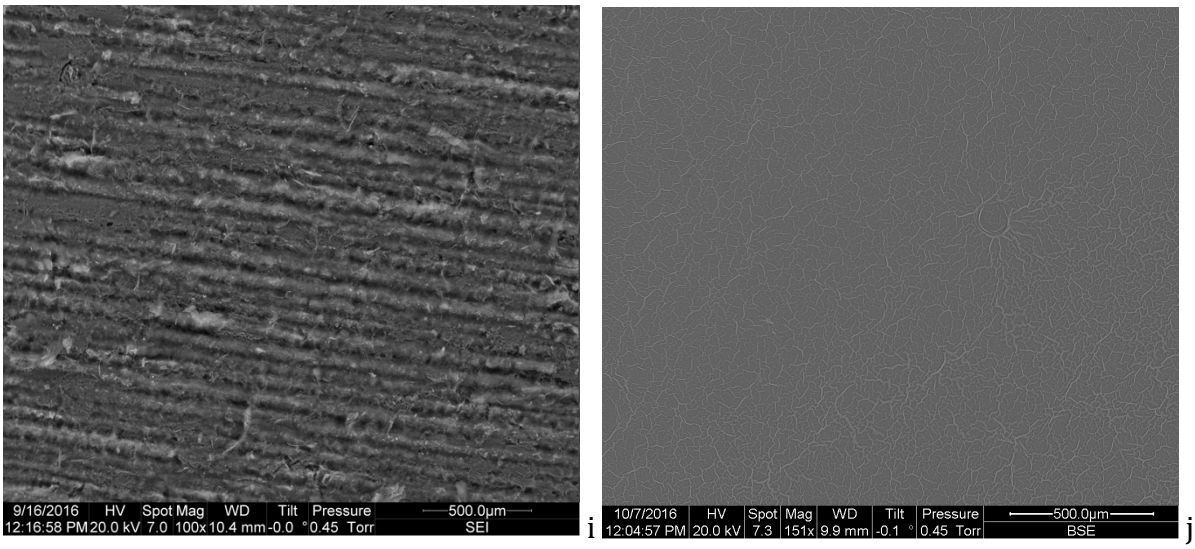

Figure 16 SEM images of rGO samples 1-9 at 100x with a scale bar of 500 µm. (a) 8 mm/s at 35 mW with 1 mm scale bar. (b) 8 mm/s at 90 mW with 1 mm scale bar. (c) 8 mm/s at 152 mW. (d) 8 mm/s at 211 mW. (e) 8 mm/s at 262 mW. (f) 8 mm/s at 308 mW. (g) 8 mm/s at 353 mW. (h) 8 mm/s at 390 mW. (i) 8 mm/s at 437 mW. (j) Unreduced graphene oxide imaged at 151x magnification with a scale bar of 500 µm.

Figure 16a shows an incomplete reduction of GO as the right hand side of the image has an approximate 50 µm wide channel of seemingly untouched GO (see **Figure 17**a). This is likely due to the fact that the beam spot at such a low power only had enough intensity for reduction at its center and wasn't able to reduce the GO under the whole beam spot. The second data point in Figure 18 confirms that the C:O ratio is only 13% greater than unreduced GO. The engraved sheet is made up of several line scans spaced 100 µm apart. Also the laser was oriented the same way for each of these samples. Taking another look at Figure 16, one can see a considerable amount of lattice defects across the rGO. Carbon dioxide and carbon monoxide gasses emitted from the GO during thermal reduction are

known to cause lattice defects (Pei & Cheng, 2011). **Figure 17** is the same set of samples (1-9) imaged on the Quanta 200 SEM at 1000x magnification.

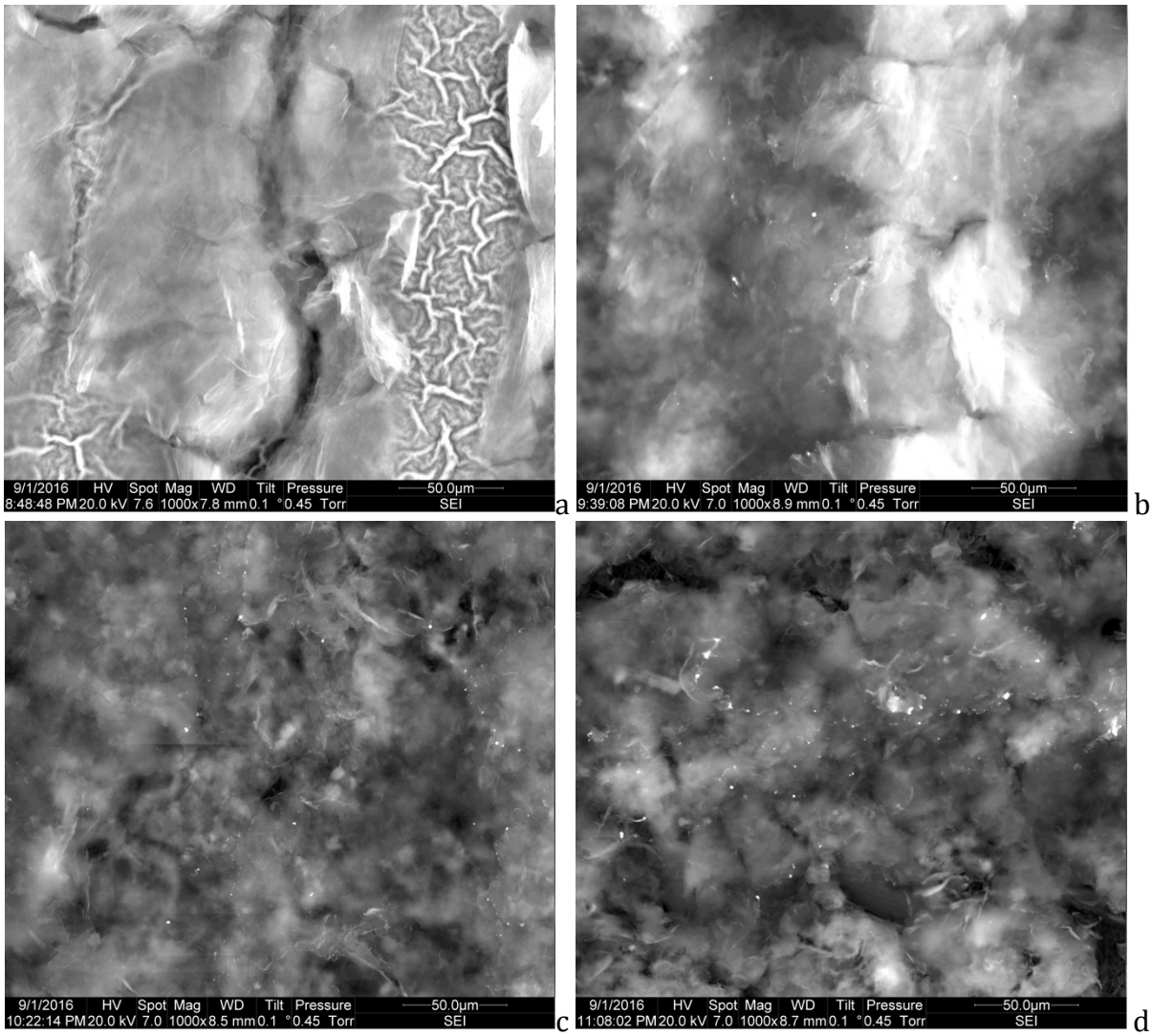

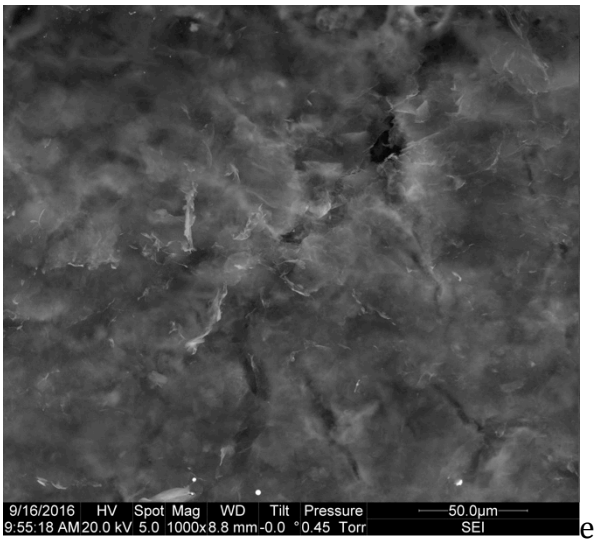
9/16/2016 HV Spot Mag WD Tilt Pressure 50.0µm
9:55:18 AM 20.0 kV 5.0 1000x 8.8 mm -0.0 ° 0.45 Torr SEI
e

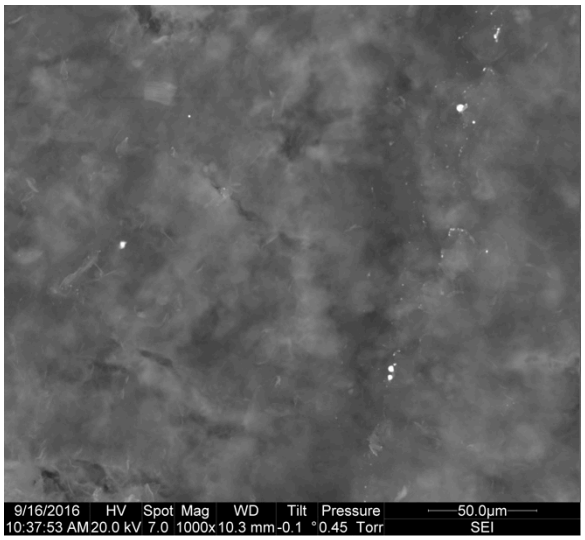
9/16/2016 HV Spot Mag WD Tilt Pressure 50.0µm
10:37:53 AM 20.0 kV 7.0 1000x 10.3 mm -0.1 ° 0.45 Torr SEI
f

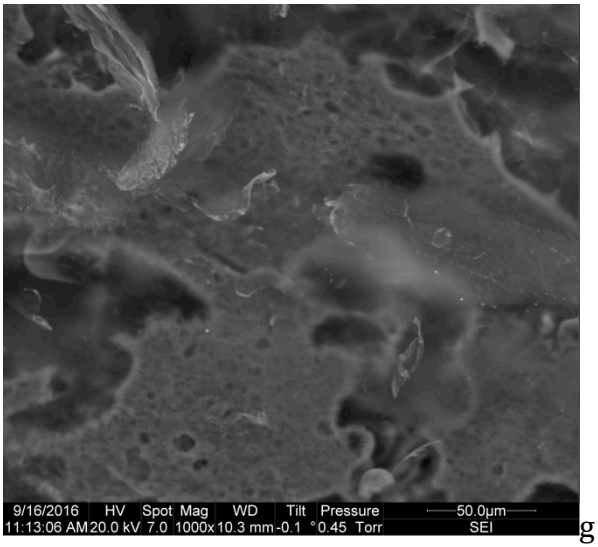
9/16/2016 HV Spot Mag WD Tilt Pressure 50.0µm
11:13:06 AM 20.0 kV 7.0 1000x 10.3 mm -0.1 ° 0.45 Torr SEI
g

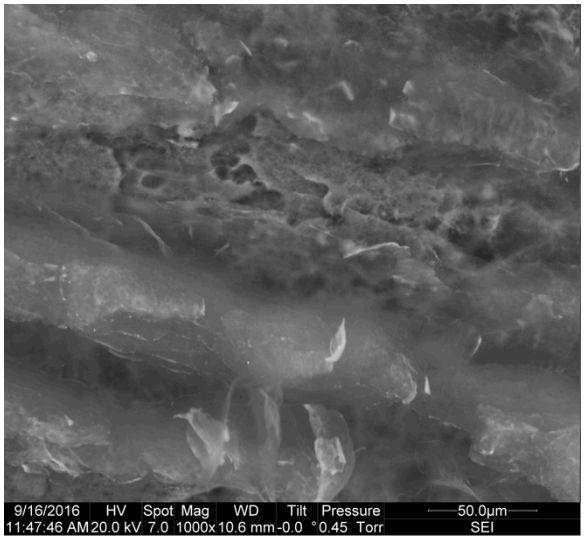
9/16/2016 HV Spot Mag WD Tilt Pressure 50.0µm
11:47:46 AM 20.0 kV 7.0 1000x 10.6 mm -0.0 ° 0.45 Torr SEI
h

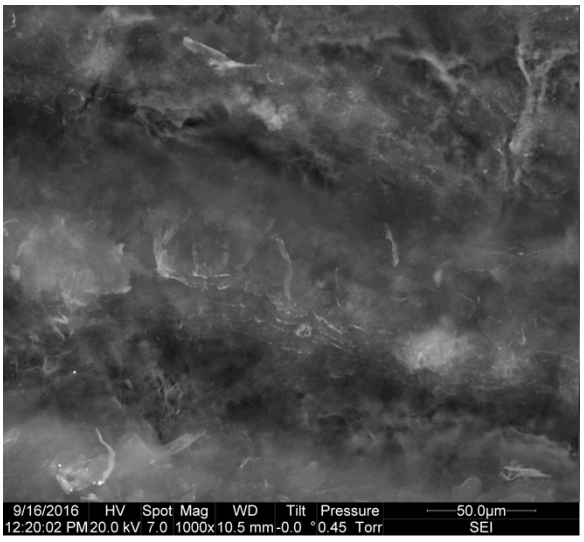

i
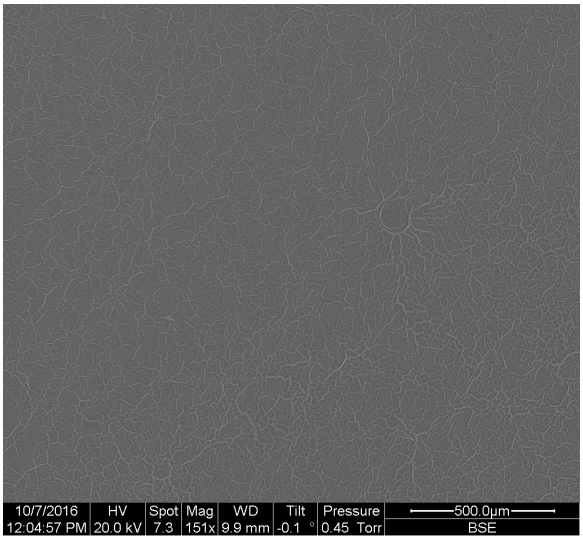

j

Figure 17 SEM images of rGO samples 1-9 at 1000x where the scale bar is 50 µm. (a) 8 mm/s at 35mW. (b) 8 mm/s at 90mW. (c) 8 mm/s at 152mW. (d) 8 mm/s at 211mW. (e) 8 mm/s at 262mW. (f) 8 mm/s at 308mW. (g) 8 mm/s at 353mW. (h) 8 mm/s at 390mW. (i) 8 mm/s at 437mW. (j) Unreduced graphene oxide imaged at 151x magnification with a scale bar of 500 µm.

Looking at the lower magnification SEM images shown in **Figure 17**, one can see more clearly the beam path of the laser as the 8.2mm by 10mm sheets of rGO are made up of several overlapping line scans.

Resistance measurements of reduced samples are consistent with reduction, but do not provide any insight on "how reduced" the rGO is. As aforementioned, the INCA X-ray microanalysis attachment to the Quanta 200 SEM was used to determine atomic ratios of the starting GO material and the final rGO product. Carbon and oxygen are the only elements present during the reduction process. Thus the carbon to oxygen ratio provides a more complete explanation of the 'degree' of reduction taking place. Figure 18 shows a plot of the carbon to oxygen ratio versus lasing power for samples 1 – 9.

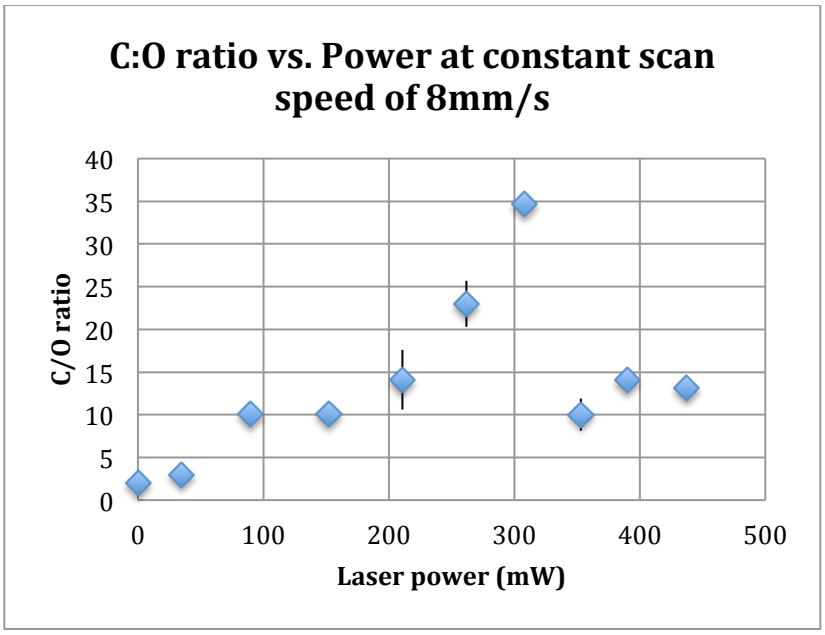

Figure 18 Carbon to oxygen ratio vs. Laser power at constant scan speed of 8 mm/s (samples 1-9). Error bars represent the standard error of the mean.

Two key facts should be noted about the above figure. The first data point in the figure represents a 2:1 carbon to oxygen ratio of unreduced GO, and C:O ratio of just the polycarbonate substrate was 5.6. As incident laser power increased, the C:O ratio also increased only for powers less than or equal to 308 mW. The last three data points (far right) do not follow the trend leading up to these points. As laser powers exceed 308 mW the resistance continues to decrease albeit slightly, and the C:O ratio quickly drops off at these powers as well. A possible explanation for this could be that when the laser reaches these higher powers, it begins to burn both the GO and the polycarbonate substrate. The result of this would lead to polycarbonate impurities to be introduced in the final rGO material. For further analysis, **Figure 19** displays a plot of resistance versus carbon to oxygen ratios of samples 1 – 9.

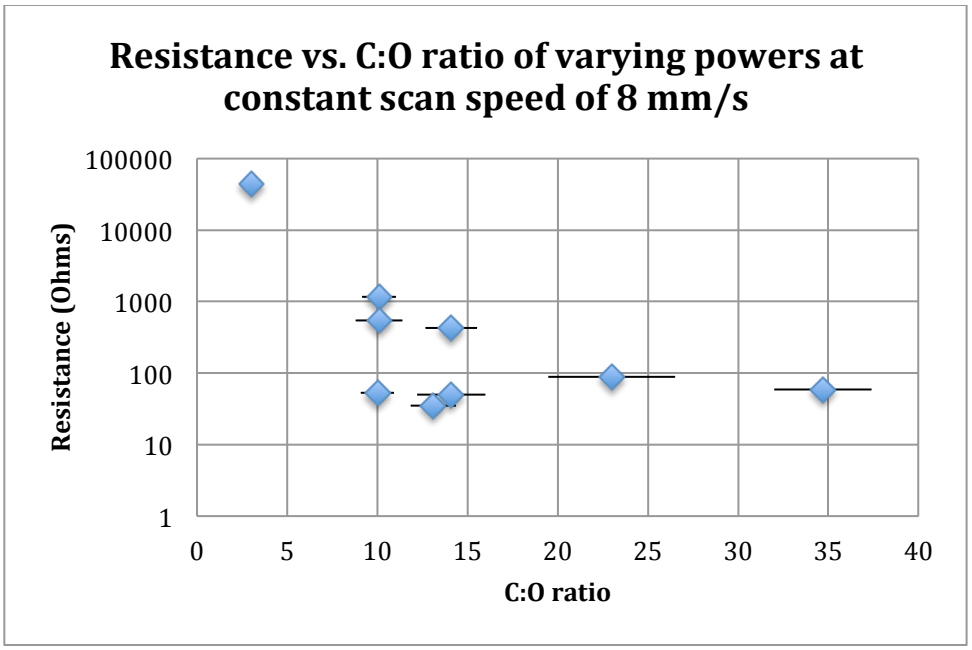

Figure 19 Resistance versus carbon to oxygen ratios of samples 1 – 9. Note the logarithmic Y-axis is used for easier interpretability. The x-axis error bars represent the standard error of the mean.

Here one can see a slight correlation between resistance and C:O ratio, but the caveat mentioned above should be kept in mind when viewing the above figure. The lowest three data points with a C:O between 10 and 15 have the lowest resistance. These three points are the engravings with the highest power (samples 7,8, and 9). **Figure 20** shows previously published data of 25-layer reduced graphene oxide sheet resistance as a function of C:O ratio (Punckt, Muckel, Wolff, Aksay, & Chavarin, 2013).

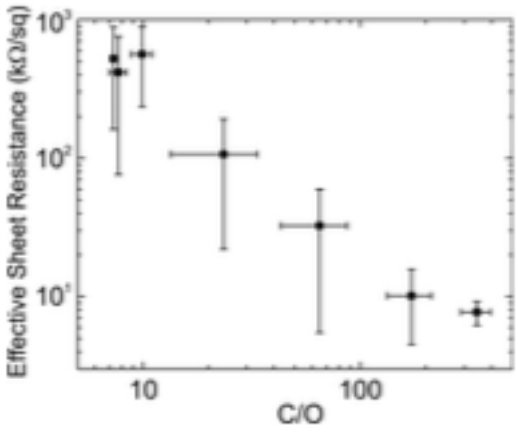

Figure 20 Sheet resistance as a function of C:O ratio (Punckt, Muckel, Wolff, Aksay, & Chavarin, 2013).

When comparing **Figure 19** to **Figure 20**, the data in this experiment does not appear to closely follow the trend in the above figure. Note that the data points in **Figure 19** can be only compared to the first four data points in **Figure 20**, as this is where the C:O ratios in both figures overlap. Also, the units on the y-axis in **Figure 20** are kΩ/sq. This is a measurement of sheet resistance, which is nothing more than a restatement of volume resistivity without specifying film thickness (Wargo). Sheet resistance is not any better at describing resistivity than a simple resistance measurement (Wargo). A better comparison can be made when viewing **Figure 19** as a log-log plot, shown in figure 21.

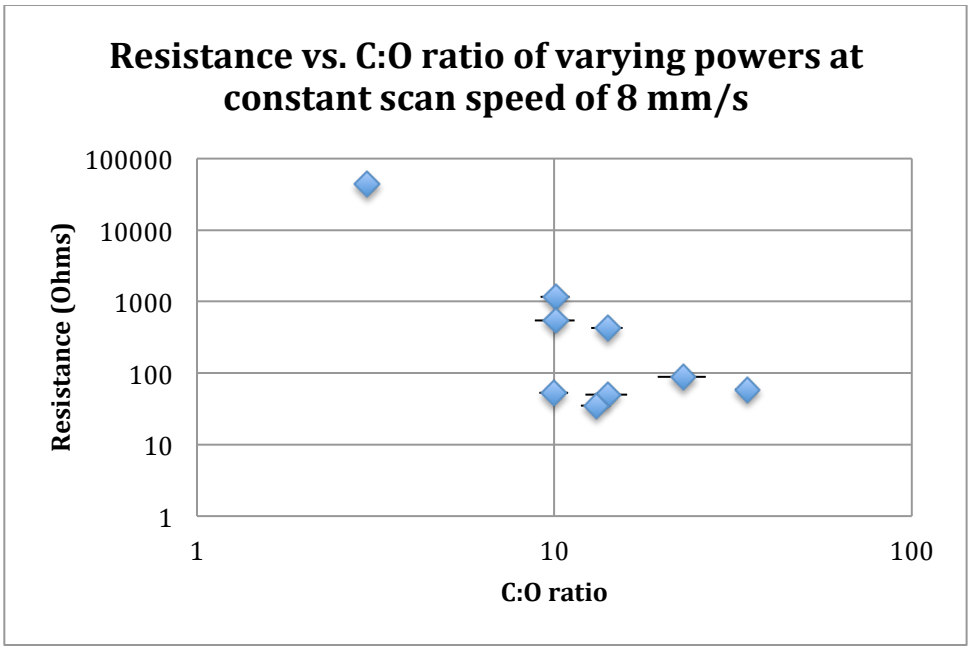

Figure 21 Resistance versus carbon to oxygen ratios of samples 1 – 9 on a log-log plot. The x-axis error bars represent the standard error of the mean.

It can be seen here that the data presented in Figure 21 is similar to the data in **Figure 20**. However, the data points in Figure 21 with the lowest three resistance values does not appear to follow the trend found in **Figure 20**; but more data must be present in both figures to confirm this assumption. The measurements in **Figure 20** were made on rGO samples prepared by chemical reduction followed by thermal reduction (Punckt, Muckel, Wolff, Aksay, & Chavarin, 2013).

5.2 - Varying Scan Speed:

Reduced graphene oxide samples 10 – 18 were studied in much the same way. Remember that samples 10 – 18 were made at a constant power of 211 mW, but with varying scan speeds of 2, 4, 6, 8, 10, 12, 16, 20, and 24 mm/second respectively. A plot of

resistance versus scan speed at a constant 211 mW lasing power is plotted and shown in **Figure 22**.

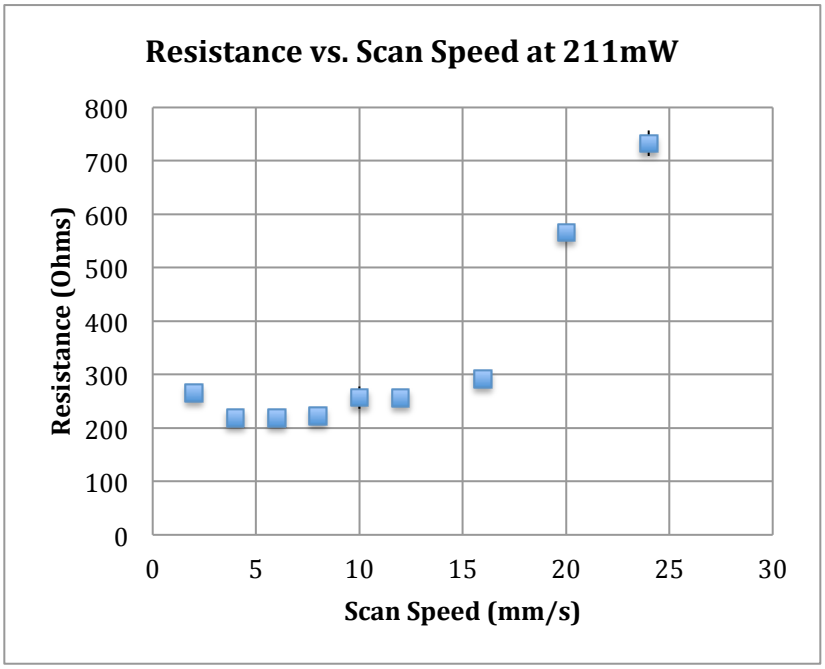

Figure 22 Resistance vs. Scan speed at constant 211mW laser power (samples 10 – 18). Error bars represent the standard error of the mean, and many are smaller than the plotted data points.

When looking at the plot above one will quickly notice that increasing scan speed leads to an increasing resistance. This is understandable considering that a slower scan speed deposits more total energy, which leads to greater reduction. Figure 23 displays the same data as **Figure 22** but plotted with a logarithmic Y-axis.

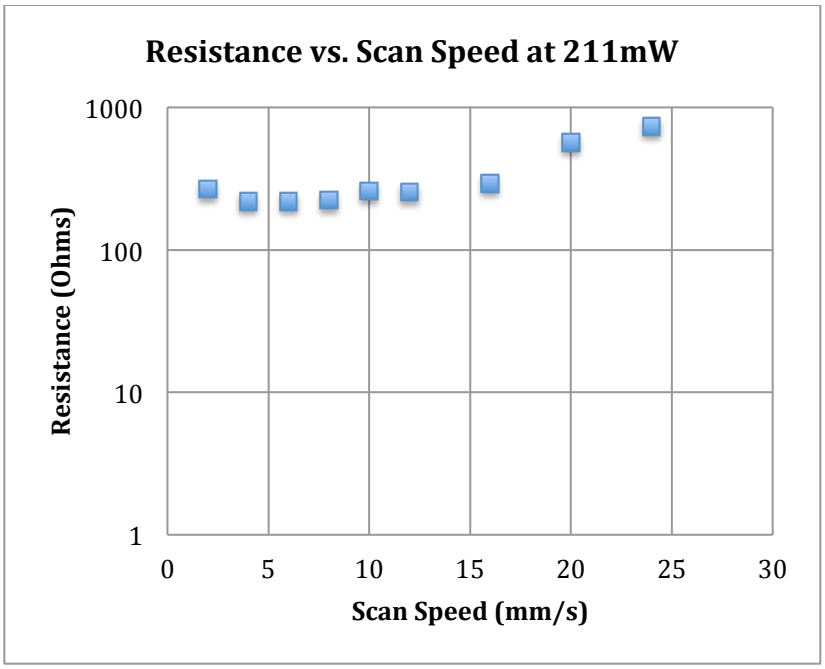

Figure 23 Resistance vs. Scan speed at constant 211mW laser power (samples 10 – 18) plotted with logarithmic Y-axis. Error bars representing the standard error of the mean, aren't visible because they are smaller than the plotted data points.

Samples 10 -18 were imaged in the same way as samples 1 – 9, and Figure 24 shows SEM images taken at 100x magnification of samples 10 -18.

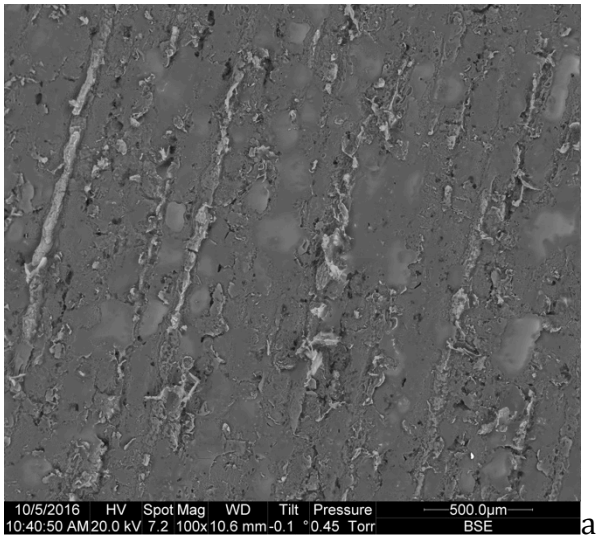

a

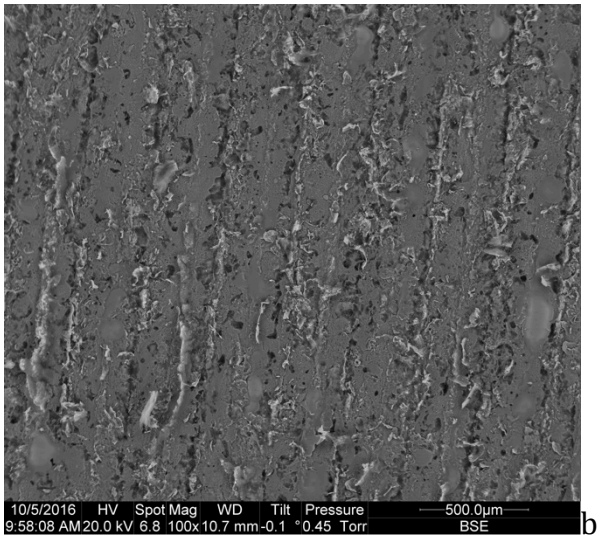

b

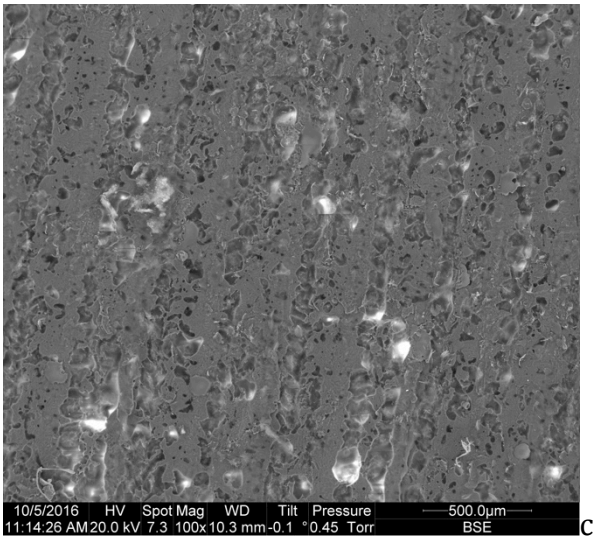
10/5/2016 HV Spot Mag WD Tilt Pressure 500.0µm
11:14:26 AM 20.0 kV 7.3 100x 10.3 mm -0.1 °0.45 Torr BSE
c

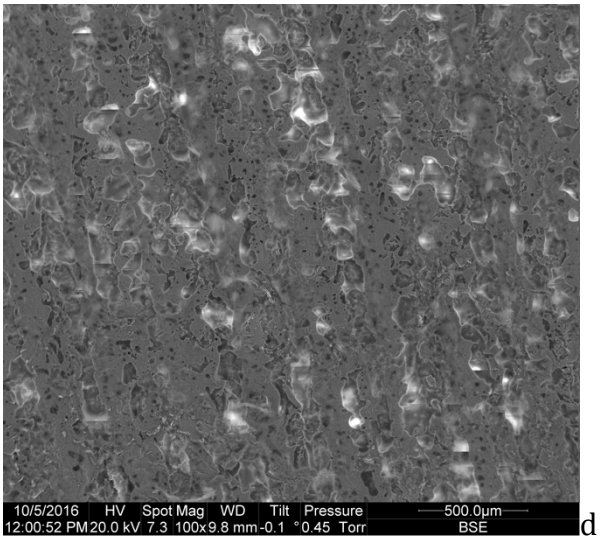
10/5/2016 HV Spot Mag WD Tilt Pressure 500.0µm
12:00:52 PM 20.0 kV 7.3 100x 9.8 mm -0.1 °0.45 Torr BSE
d

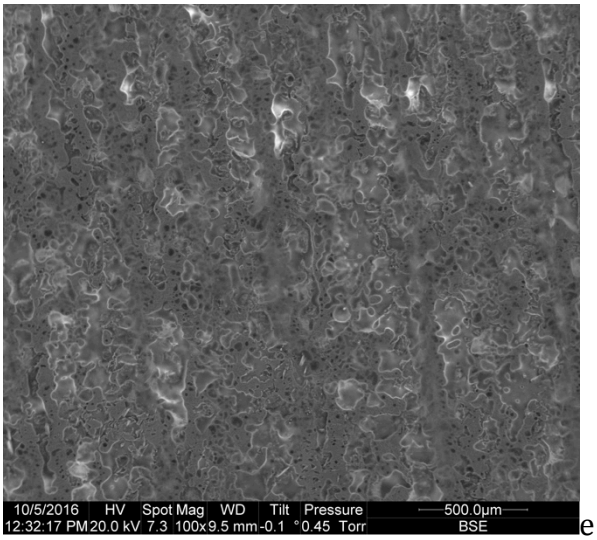
10/5/2016 HV Spot Mag WD Tilt Pressure 500.0µm
12:32:17 PM 20.0 kV 7.3 100x 9.5 mm -0.1 °0.45 Torr BSE
e

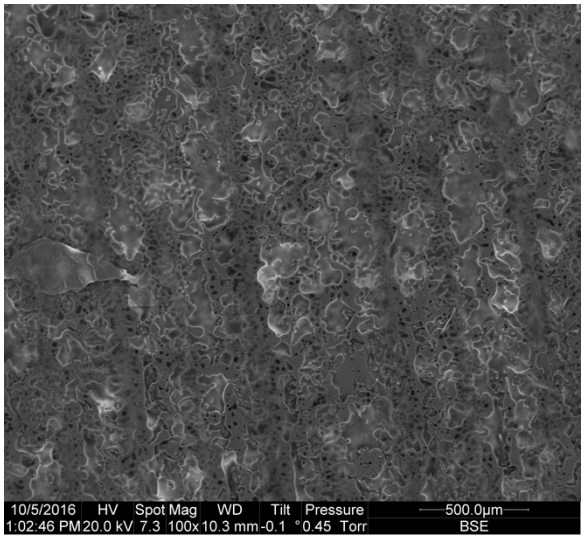
10/5/2016 HV Spot Mag WD Tilt Pressure 500.0µm
1:02:46 PM 20.0 kV 7.3 100x 10.3 mm -0.1 °0.45 Torr BSE
f

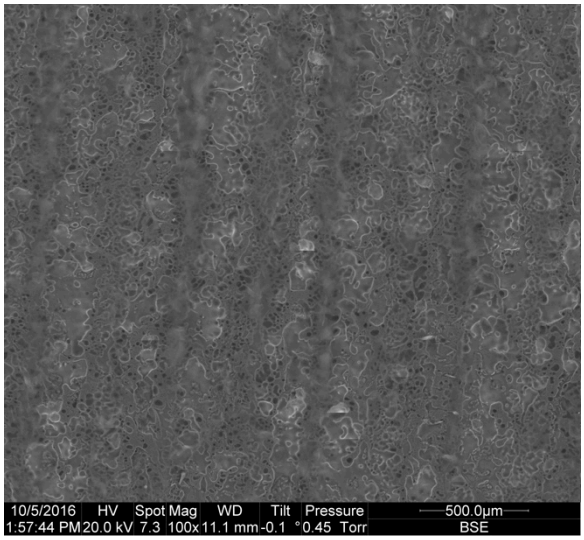
10/5/2016 HV Spot Mag WD Tilt Pressure 500.0µm
1:57:44 PM 20.0 kV 7.3 100x 11.1 mm -0.1 °0.45 Torr BSE
g

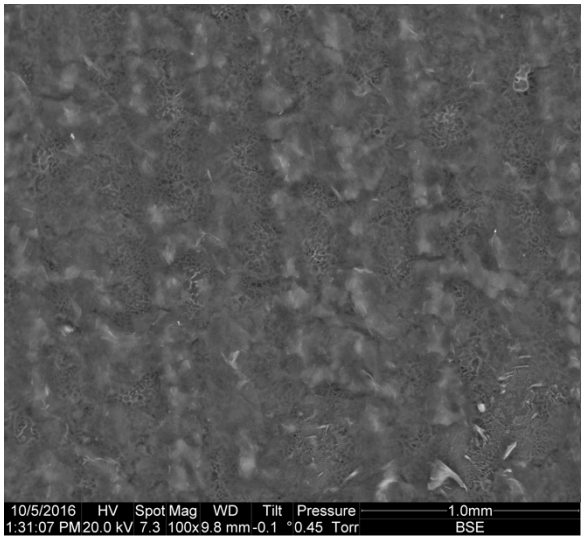
10/5/2016 HV Spot Mag WD Tilt Pressure 1.0mm
1:31:07 PM 20.0 kV 7.3 100x 9.8 mm -0.1 °0.45 Torr BSE
h

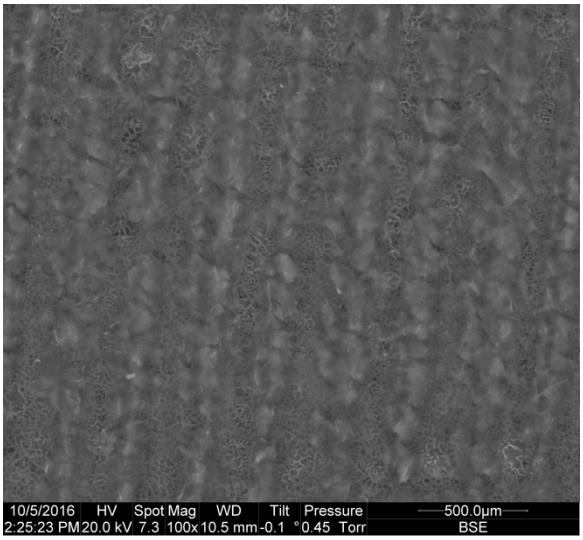

j

Figure 24 SEM images of rGO samples 10 - 18 at 100x with a scale bar of 500 µm. (a) 2 mm/s at 211 mW. (b) 4 mm/s at 211 mW. (c) 6 mm/s at 211 mW. (d) 8 mm/s at 211 mW. (e) 10 mm/s at 211 mW. (f) 12 mm/s at 211mW. (g) 16 mm/s at 211 mW. (h) 20 mm/s at 211 mW. (i) 24 mm/s at 211 mW.

As mentioned earlier, the structural defects seen here are likely due to the evolution of carbon dioxide and carbon monoxide gases emitted upon reduction. SEM images of samples 10 – 18, taken at a smaller scale at 1000x magnification are shown below in Figure 25.

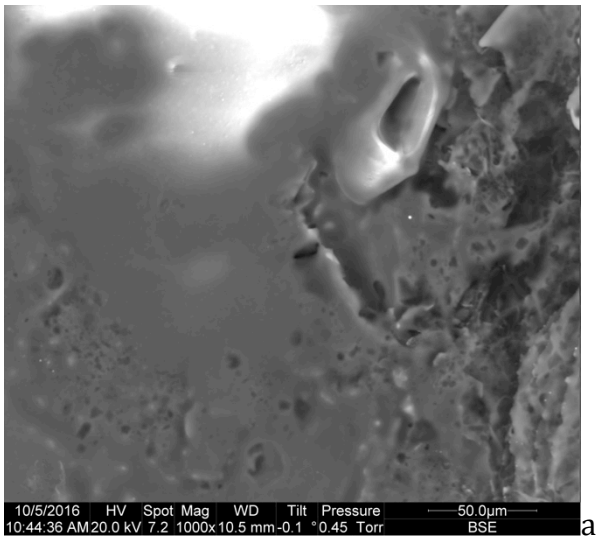
10/5/2016 HV Spot Mag WD Tilt Pressure 50.0µm
10:44:36 AM 20.0 kV 7.2 1000x 10.5 mm -0.1 °0.45 Torr BSE
a

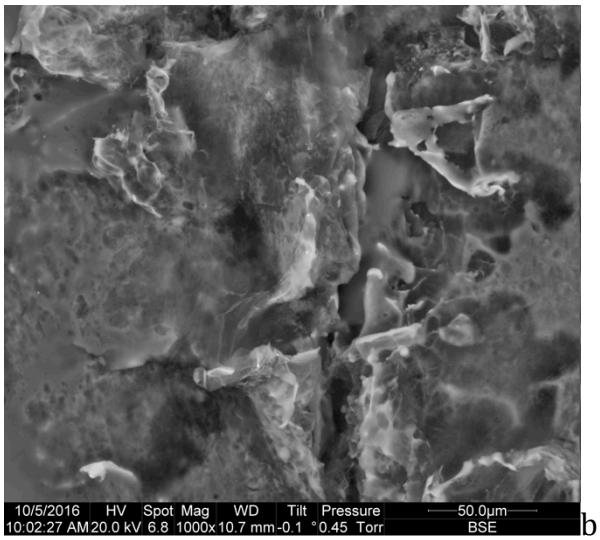
10/5/2016 HV Spot Mag WD Tilt Pressure 50.0µm
10:02:27 AM 20.0 kV 6.8 1000x 10.7 mm -0.1 °0.45 Torr BSE
b

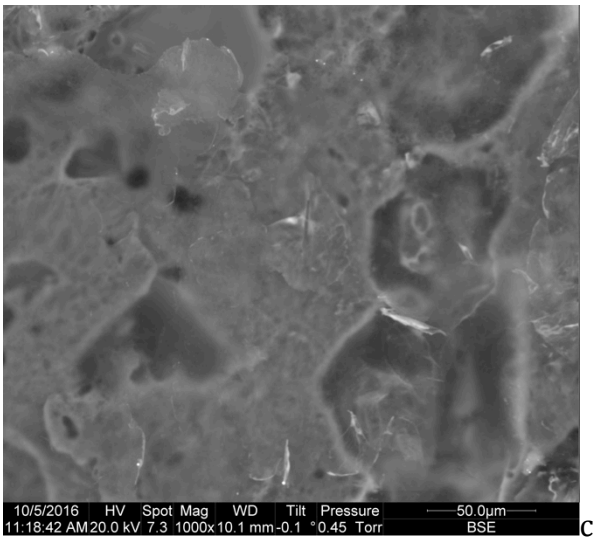
10/5/2016 HV Spot Mag WD Tilt Pressure 50.0µm
11:18:42 AM 20.0 kV 7.3 1000x 10.1 mm -0.1 °0.45 Torr BSE
c

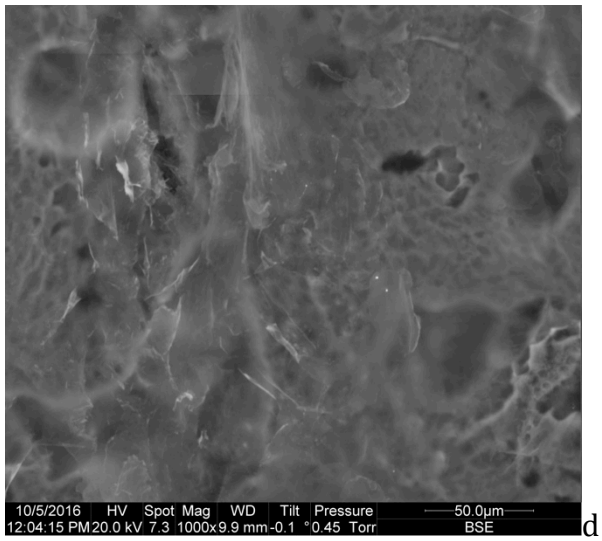
10/5/2016 HV Spot Mag WD Tilt Pressure 50.0µm
12:04:15 PM 20.0 kV 7.3 1000x 9.9 mm -0.1 °0.45 Torr BSE
d

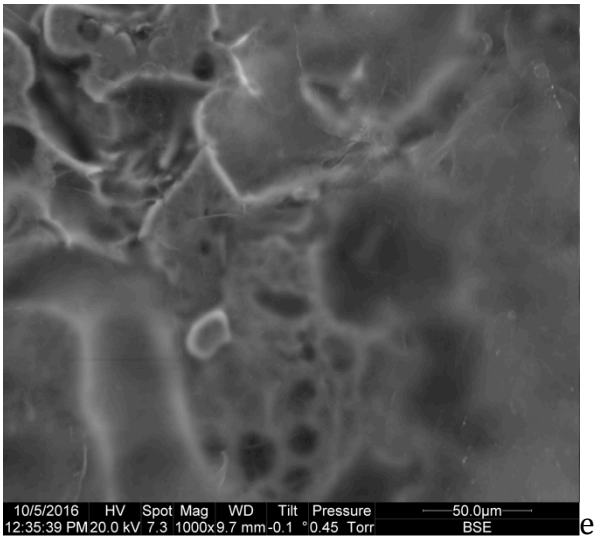
10/5/2016 HV Spot Mag WD Tilt Pressure 50.0µm
12:35:39 PM 20.0 kV 7.3 1000x 9.7 mm -0.1 °0.45 Torr BSE
e

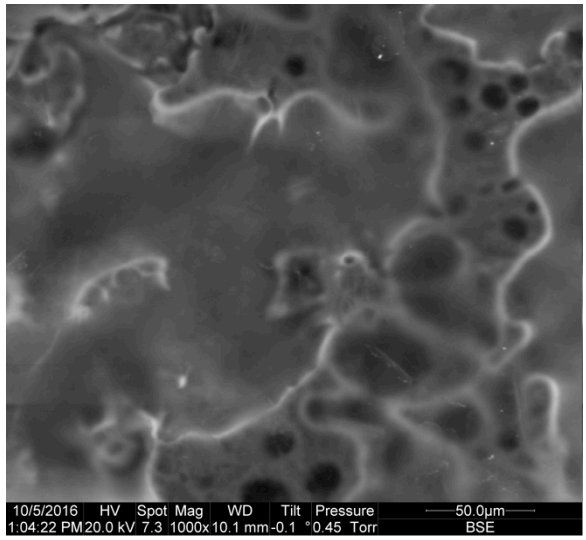
10/5/2016 HV Spot Mag WD Tilt Pressure 50.0µm
1:04:22 PM 20.0 kV 7.3 1000x 10.1 mm -0.1 °0.45 Torr BSE
f

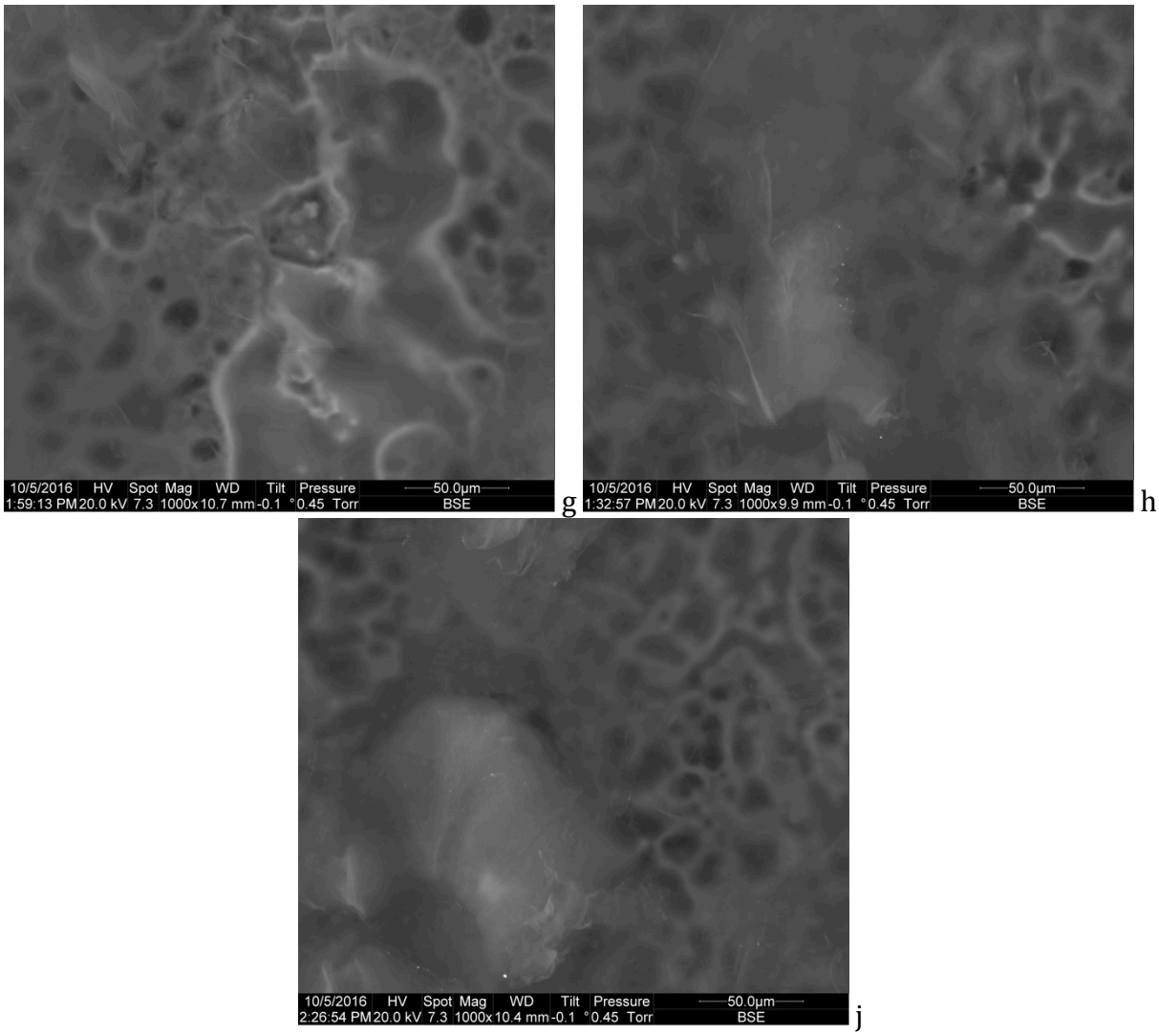

Figure 25 SEM images of rGO samples 10 - 18 at 1000x with a scale bar of 50 microns. (a) 2 mm/s at 211 mW. (b) 4 mm/s at 211 mW. (c) 6 mm/s at 211 mW. (d) 8 mm/s at 211 mW. (e) 10 mm/s at 211 mW. (f) 12 mm/s at 211 mW. (g) 16 mm/s at 211 mW. (h) 20 mm/s at 211 mW. (i) 24 mm/s at 211 mW.

Similarities of rGO texture can be observed in samples 10 and 11. Similarities in samples 12 through 16 can also be seen, as the rGO product seems to have a porous like texture.

Samples 17 and 18, made at 20 mm/s and 24 mm/s show more of the lined patterning characteristic of lower energy deposition (see Figure 24).

Following along with the analysis, the carbon to oxygen ratios of rGO samples 10 – 18 were taken and plotted as a function of scan speed and shown in Figure 26.

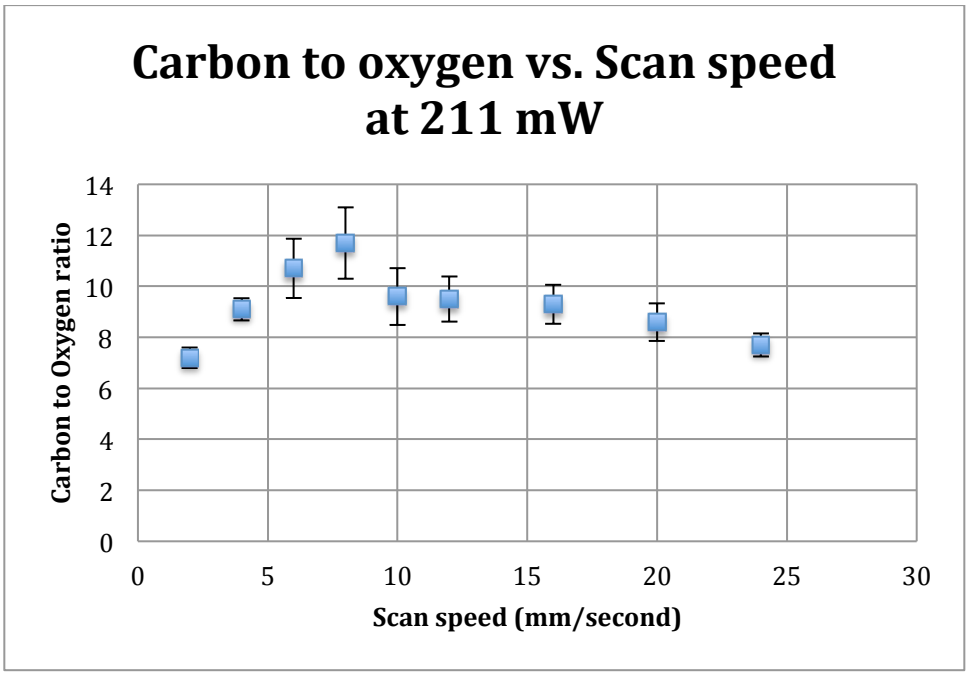

Figure 26 carbon to oxygen ratio versus scan speed at a constant 211 mw lasing power. Error bars represent the standard error of the mean.

In Figure 26 the C:O ratio increases from scan speeds 2 mm/s through 8 mm/s, and then a shallow decrease in C:O ratio happens at scan speeds exceeding 8 mm/s.

To supplement this analysis, Figure 27 shows a plot of resistance versus carbon to oxygen ratio of rGO samples 10 – 18.

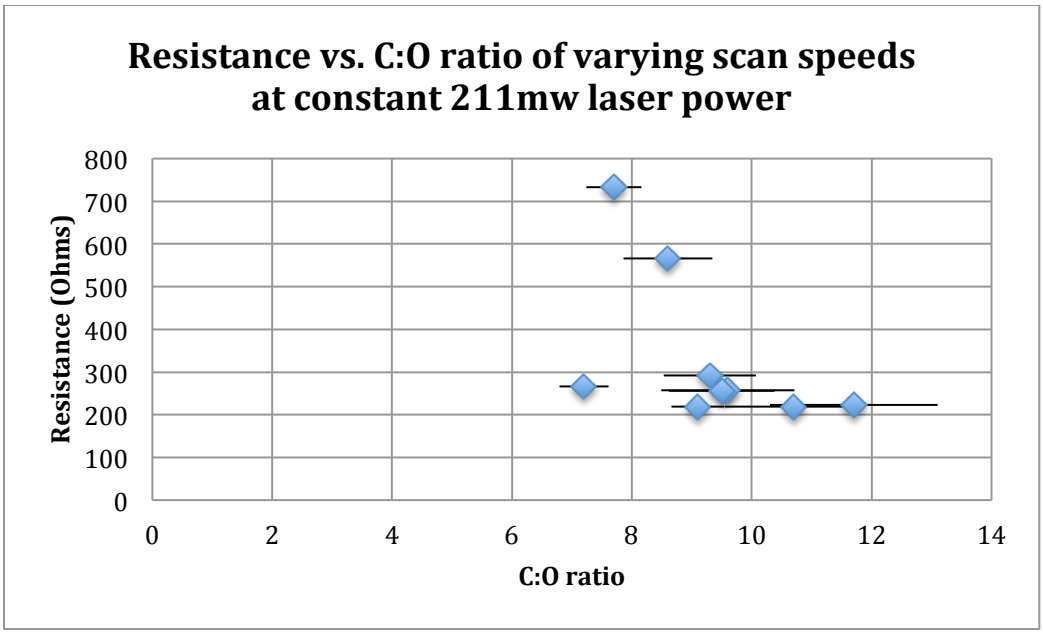

Figure 27 Resistance versus carbon to oxygen ratio of samples 10 - 18. The x-axis error bars represent the standard error of the mean.

In viewing Figure 27, it is apparent that there is little correlation between resistance and C:O ratio when varying scan-speed (i.e. total energy deposited) at a constant laser power of 211mW. Also when comparing the figure above with **Figure 20**, it can bee seen that this plot does follow the trend found in **Figure 20**. Let us look at Figure 27 on a log-log plot to have a more clear comparison.

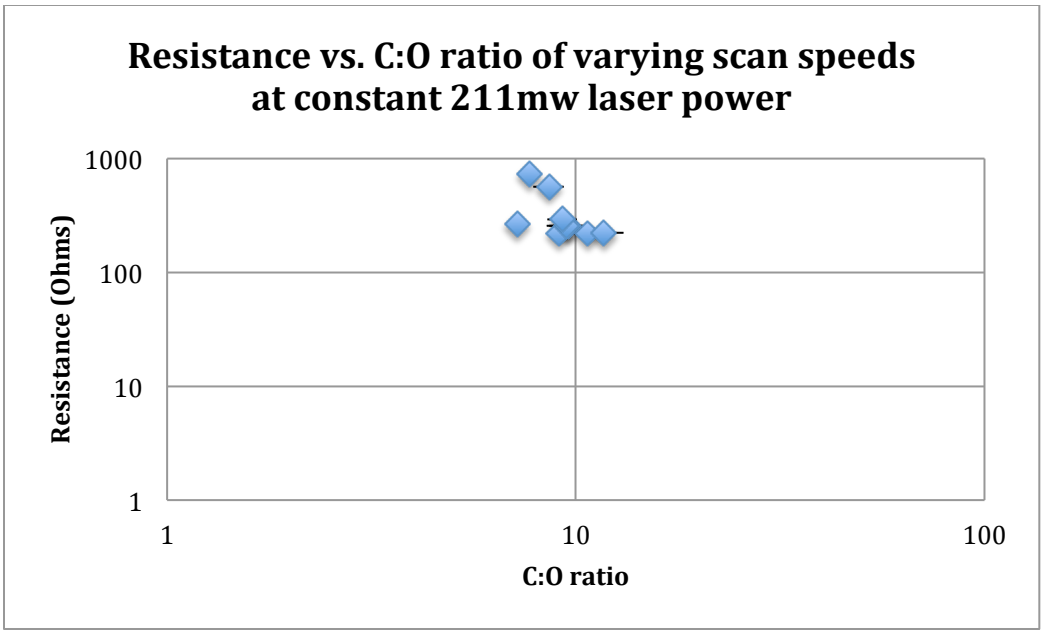

Figure 28 Resistance versus carbon to oxygen ratio of samples 10 – 18 on a log-log plot. The x-axis error bars represent the standard error of the mean.

In viewing the log-log plot above and comparing it to **Figure 20** the data points in both plots are clustered around a C:O of 10, and a clear trend cannot be found. Also, the data point farthest to the left in Figure 27 was the sample that was scanned at 2 mm/s. This data point is consistent with the hypothesis that the polycarbonate substrate introduces oxygen impurities to the rGO. This sample experienced the most exposure and highest total energy deposited.

5.3 – Constant Total Energy Deposition:

Finally, rGO samples 19 – 24 were made at varying scan speeds of constant laser power, but with same total energy of 98 joules deposited for each sample. This was done by scanning sample 19 once at 2 mm/s, sample 20 twice at 4 mm/s, sample 21 three times

at 6 mm/s, sample 22 four times at 8 mm/s, sample 23 five times at 10 mm/s, and sample 24 six times at 12 mm/s. A plot of resistance versus scan speed is shown in Figure 29.

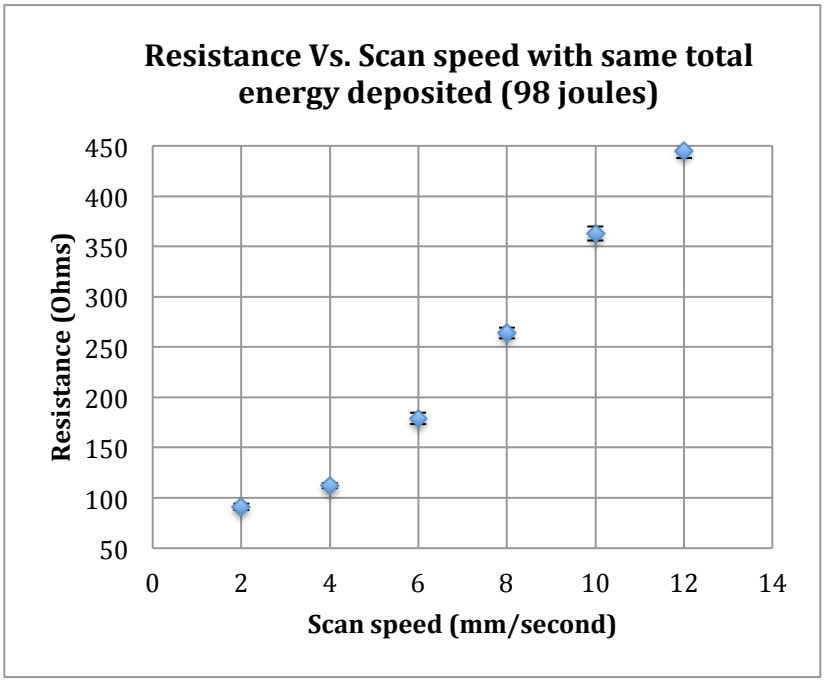

Figure 29 Resistance vs. Scan speed with necessary number of rescans to achieve same total energy of 98 joules for each sample (19 – 24). The error bars represent the standard error of the mean.

Figure 29 clearly shows that optimal resistance is achieved by a single scan at a slow scan speed. Now is a good time to point out that this data is inconsistent with the data in figure 18 where a 2 mm/s scan speed did not achieve the best resistance. The trend in Figure 29 is likely due to the fact that the sample is allowed to 'cool' between rescans, limiting the amount of reduction taking place.

Further observations found can estimate some important quantities pertaining to temperature pertaining to this experiment. Firstly, when the rGO and GO was cleaned from

the substrate, an indention was seen where the laser was scanned. Since the polycarbonate substrate began to melt during lasing, this indicates that a minimum temperature of 288 ^{o}C (melting point of polycarbonate (RTP Company)) was reached upon reduction. Also, because the concentration and volume of the aqueous GO dispersion is known, an estimate of thickness can be calculated given that about 0.65 grams of GO per square centimeter was present on the drop casted sample. The density of GO is approximately 1.8 g/cm^3 (Sigma-Aldrich), which leads to a rough thickness calculation of about 3.6 microns.

When comparing resistance as a function of power and resistance as a function of scan speed the data shows an interesting phenomenon. Joule for joule, a higher power at a faster scan speed produced better resistances than a lower power at a slower scan speed, when equivalent total energies were deposited. This means that energy density of the laser is more closely connected to lower resistances. The data gathered for carbon to oxygen ratios as a function of power and as a function of scan speed tell a different story. At equivalent total energy deposition, slower scans at lower power produces higher C:O ratios up to 24.3 joules deposited. At total energies greater than 24.3 joules, faster scan speeds at higher powers yields higher C:O ratios. This holds true for up to 50 joules, and beyond that, more experimental data must be gathered to confirm if this trend continues or if it changes.

Since each sample plotted in Figure 29 has different resistances despite the same total energy deposited (98 joules), it can be concluded that reduction quality of rGO in this experiment is better connected to temperature than total energy deposition. Using a thermally conductive substrate yields no measurable changes to the GO, and is another indication that reduction is more dependent on temperature.

5.4 – Conclusion:

Areas where this research can be expanded are important to mention for anyone interested in laser reduction of GO. Firstly, a higher power laser could be used to broaden the power ranges studied in the section above. Also this same analysis can be used to examine reduction quality on a variety of substrates, which may lead to a better correlation between C:O ratio and resistance. When characterizing GO and rGO, it would be beneficial to use more spectroscopy to determine exactly which functional groups are present before and after reduction. An attempt at using Attenuated Total Reflection (ATR) spectroscopy was made. However, a proper ATR spectrum could not be obtained because the refraction index of the diamond ATR crystal was lower than that of the sample. Thus, the critical angle necessary for total internal reflection could not be met. Using a Germanium crystal in the ATR would provide an accurate spectrum. Also, measuring the thickness of the rGO would allow for proper resistivity and conductivity calculations to be made. Furthermore, researchers in 2009 state that for thermal reduction to take place temperatures must exceed 1000 ^{o}C (Punckt, Muckel, Wolff, Aksay, & Chavarin, 2013). An infrared video microscope would provide a temperature map to verify that the laser used in this experiment reaches temperatures greater than 1000 ^{o}C.

The goal for this research was to optimize a single step laser reduction process of on-substrate graphene oxide. The lowest resistance achieved in this research was 35 Ohms, using 437 mW lasing power at 8 mm/s scan speed. A carbon to oxygen ratio of 34.7 was the highest ratio obtained in this experiment, produced by 308mW of 450nm irradiation at 8 mm/s scanning speed. This C:O ratio is noteworthy because on-substrate thermal reduction of GO has not been shown to yield a ratio of greater than 14 (Punckt,

Muckel, Wolff, Aksay, & Chavarin, 2013). Of the data presented in chapter 5, scan speed did not have nearly as significant of an effect on resistance as power did; because increasing power increases energy density which has a more significant effect on temperature.

Single step laser reduction of GO is an extremely cost effective way to produce graphene like electronics. The research in this paper was done with less than $100 including the CNC build. Using a laser reducing method, one can customize his or her 2D electronic circuits and can even vary resistance during engraving by altering the lasing power or scan speed. Carbon based electronics are also highly recyclable and can be repurposed to meet a variety of needs (Murray-Smith, 2013). Reduced graphene oxide circuits are pliable and can be used for wearable electronics that measure biometrics by exploiting performance changes when under strain.

REFERENCES

Balandin, A. A., Ghosh, S., Bao, W., Calizo, I., Teweldebrhan, D., Miao, F., et al. (2008). Superior Thermal Conductivity of Single-Layer Graphene. *Nano letters* , 902-907.

Campos-Delgado, J., Kim, Y., Hayashi, T., Morelos-Gómez, A., Hofmann, M., Muramatsu, H., et al. (2009). Thermal stability studies of CVD-grown graphene nanoribbons: Defect annealing and loop formation. *Chemical Physics Letters , 469* (1-3), 177-182.

Chua, C. K., & Pumera, M. (2014). Chemical reduction of graphene oxide: a synthetic chemistry viewpoint. *The Royal Society of Chemistry 2014 , 43*, 291-312.

City Plastics. (n.d.). *Polycarbonate*. Retrieved December 4, 2016, from cityplastics.com: http://www.cityplastics.com.au/materials-polycarbonate/

Douglas, I. (2014, June 18). *A Raspberry Pi controlled mini CNC Laser engraver*. Retrieved July 30, 2014, from funofdiy.blogspot.com: http://funofdiy.blogspot.com/2013/10/a-raspberry-pi-controlled-mini-laser.html

El-Kady, M. F., Strong, V., Dubin, S., & Kaner, R. B. (2012). Laser Scribing of High-Performance and Flexible Graphene-Based Electrochemical Capacitors. *Science , 335*, 1326-1330.

Geim, A., & Novoselov, K. (2010, October). The Nobel Prize in Physics 2010. *The Royal Swedish Academy of Sciences* .

Lee, C., Wei, X., Kysar, J. W., & James, H. (2008). Measurement of the Elastic Properties and Intrinsic Strength of Monolayer Graphene. *Science* , 385-288.
Liu, Y., Xie, B., Zhang, Z., Zheng, Q., & Xu, Z. (2012). Mechanical Properties of Graphene Papers. *Journal of the Mechanics and Physics of Solids* , 591-605.

Mendoza, D. (2012). Electrical Conductivity of Collapsed Multilayer Graphene Tubes. *WJNSE , 2*, 53-57.

Murray-Smith, R. (2013). *Graphene 101 - An Inventors Guide to Making Graphene.* Smashwords.

Pei, S., & Cheng, H.-M. (2011). The reduction of graphene oxide. *Carbon , 50*, 3210-3228.

Punckt, C., Muckel, F., Wolff, S., Aksay, I. A., & Chavarin, C. A. (2013). The effect of degree of reduction on the electrical properties of functionalized graphene sheets. *Applied Physics Letters , 102*.

RTP Company. (n.d.). *Product Data Sheet Polycarbonate Unreinforeced.* Retrieved December 4, 2016, from rtpcompany.com: http://web.rtpcompany.com/info/data/0300/RTP300.htm

Sigma-Aldrich. (n.d.). *Graphene Oxide*. Retrieved December 4, 2016, from sigmaaldrich.com: http://www.sigmaaldrich.com/catalog/product/aldrich/796034?lang=en&region=US

Wargo, C. (n.d.). *Characterization of Conductors for Printed Electronics*. Retrieved December 6, 2016, from nanopchem.com: http://www.nanopchem.com/pdf/understanding.pdf

Yang, D., Velamakanni, A., Bozoklu, G., Park, S., Stoller, M., Piner, R. D., et al. (2009). Chemical analysis of graphene oxide films after heat and chemical treatments by X-ray photoelectron and Micro-Raman spectroscopy. *Carbon , 41* (1), 145-152.